International Journal of Robotics and Control Systems
Vol. 5, No. 6, 2025, pp. 2889-2917
ISSN 2775-2658
http://pubs2.ascee.org/index.php/ijrcs

Intelligent Longitudinal Control for PMSM-Based Autonomous Vehicles Using YOLOv10-S and a Fuzzy-PI Controller

Elhoussein Elouardi [a,1,*], Mohamed Zarboubi [b,2], Hicham El Aiss [c,3], Abdelkader Mezouari [a,4], Hamad Dahou [a,5], Elouardi Brahim [d,6], Omar Mouhib [a,7]

[a] Laboratory of Electrical Engineering and Energy Systems, Faculty of Sciences, Ibn Tofail University, Kénitra, Morocco
[b] LISAD Laboratory, National School of Applied Sciences, Ibn Zohr University, Agadir, Morocco
[c] Department of Electrical Engineering, University of Santiago of Chile, Chile Identification and Control Laboratory, Chile
[d] Department of Physics, LPMC-ERSA, Faculty of Sciences Ben M'sik, University Hassan II, B.P 7955, 20800 Casablanca, Morocco
[1] elhoussein.elouardi1@uit.ac.ma; [2] mohamed.zarboubi@edu.uiz.ac.ma; [3] hicham.elaiss@usach.cl;
[4] abdelkader.mezouari@uit.ac.ma; [5] hamad.dahou@uit.ac.ma; [6] smp-enspc5@hotmail.com; [7] omar.mouhib@uit.ac.ma
[*] Corresponding Author

ARTICLE INFO

Article history
Received June 07, 2025
Revised August 24, 2025
Accepted December 06, 2025

Keywords
Autonomous Vehicle;
YOLOv10;
LQR;
LILF;
H∞ Control

ABSTRACT

This study presents an intelligent longitudinal control system for autonomous electric vehicles using permanent magnet synchronous motors (PMSMs). The system integrates real-time traffic sign recognition with advanced control strategies to improve speed regulation, energy efficiency, and ride comfort. A lightweight YOLOv10-S model is trained to accurately and quickly detect speed limit signs under diverse conditions. The detected speed is used as a reference input for a fuzzy PI controller designed using two approaches: a Linear Quadratic Regulator (LQR) and a robust H∞ strategy based on a Linear Integral Lyapunov Function (LILF) via Linear Matrix Inequalities (LMI). Simulation results highlight that the YOLOv10-S model achieves high accuracy with low detection losses and strong mAP scores across IoU thresholds (0.5–0.95). The proposed control system demonstrates clear advantages over traditional PID and LQR controllers. The LILF-based controller achieves a rise time of 5 ms, zero overshoot, zero steady-state error, and complete rejection of load-induced vibrations. Meanwhile, the LQR controller ensures energy-efficient operation with a 9 ms rise time and reduced current consumption. By integrating deep learning perception with robust control techniques, this system enables autonomous vehicles to dynamically adapt to traffic regulations, resulting in more accurate speed tracking, smoother driving, and lower energy consumption, key benefits for real-world electric mobility.

1. Introduction

The transportation sector plays a fundamental role in human life. It facilitates the movement of people and goods at local, national, and international levels. However, it presents significant challenges, such as safety, environmental impact, and urban congestion [1]. According to the World Health Organization (WHO), it is estimated that approximately 1.19 million people will die in 2023

as a result of road accidents [2]. In light of this alarming statistic, it becomes evident that traditional longitudinal control of vehicles, which relies solely on driver input to manage speed and braking, has significant limitations. These systems are heavily dependent on human perception and reaction time, making them vulnerable to errors, especially in complex or rapidly changing traffic conditions. As a result, there is an increasing need to adopt intelligent longitudinal control systems that utilize real-time data, automation, and adaptive algorithms. These advanced systems can assist or even take over certain driving functions, leading to improved safety, better traffic efficiency, and a reduction in accident rates.

In this context, thanks to advancements in artificial intelligence, autonomous vehicles (AVs), aim to improve urban sustainability and safety by interacting seamlessly with infrastructure and the environment [3]. Indeed, recent advancements in machine vision and deep learning (DL) algorithms, particularly convolutional neural networks (CNNs), play a crucial role in diverse domains, from agriculture to transportation [4]–[6]. These algorithms are credited with the emergence and evolution of autonomous vehicles. CNN-based object detectors, such as You Only Look Once (YOLO) [7], SSD [8], Cascade R-CNN [9], Faster R-CNN [10], and Fast R-CNN [11], have shown exceptional capability in detecting and recognizing traffic signs in self-driving mode. These signs are indispensable for real-time decision-making, ensuring the safety and reliability of autonomous vehicles in dynamic and unpredictable environments [12]–[14].

Among the available object detection technologies, YOLO stands out for its real-time responsiveness and accuracy, making it a cornerstone of modern autonomous systems. Notably, ten iterations of the YOLO algorithm—ranging from YOLOv1 to YOLOv10 [15]–[23]—have successively enhanced performance metrics, providing robust and efficient solutions to complex detection tasks. Traffic sign detection, as a use case of object detection, mirrors the challenges tackled in other domains, such as insect counting in agriculture, where CNNs have similarly proven to be optimal solutions [14]. In the transportation sector, region proposal-based and regression methods remain dominant strategies, yet YOLO's ability to process information with both precision and speed has led to its widespread adoption. This progress underscores the vital role of robust object detection models in addressing global challenges such as road safety and urban mobility. Leaders in this space must recognize that the accurate identification and interpretation of objects within a scene are not just technical requirements but foundational enablers for building smarter and safer transportation systems.

Nevertheless, the transportation of the future must be integrated into a global environmental framework focused on enhancing energy efficiency and combating climate change by reducing greenhouse gas emissions [24]. The integrity of AV in the future transport system must be aligned with contemporary autonomous and electric structures [25]. The dual-function of the motor as it pertains to vehicle motion predetermines that engine as the central focus distinguishing an internal combustion vehicle from an electric vehicle. But there are electric machines that belong to the class of electric motors, and there is quite a difference in performance based on control strategies employed. Permanent Magnet Synchronous Motors are considered the most popular class of motors for electric vehicles due to their high efficiency, good power density, high torque-to-inertia ratio, and volume-to-weight ratio. Besides, slip-less configurations make these motors very effective in speed control and load variations compared to other motor types [26]–[28]. Challenges in respect of safety and energy management, though, remain to delay the integration of these vehicles into sustainable mobility.

The field of electrical machine control has developed considerably over these last decades. Several control techniques, such as Predictive Control (MPC) [29], Direct Torque Control (DTC) [30], [31], Direct Flux Orientation Control (DFOC) [32], Fuzzy Logic Control [33], [34], Sliding Mode Control (SMC), etc. [35] have been developed to reduce periodic torque ripples in polyphase machines, which in turn lead to speed oscillations and may damage the machine.

The regulation of vehicles through control over motor management that would be represented by the PMSM is lucidly declared to be of utmost use in ensuring by any means the stabilization and safety essential for the vehicle concerned under uneven road conditions. The sinusoidal control method for

PMSM motors is a simple approach where the supply voltage vector is 90 degrees offset from the rotor flux axis. This method reduces torque ripple and allows precise shaft control [36]–[39]. However, the assumption of a constant angle between the voltage vector and rotor flux limits maximum torque due to phase discrepancies between current and voltage. The Field Oriented Control (FOC) method delivers better results; however, it has the drawback of requiring continuous measurement of motor currents and adjustment of the supply voltage to control both the torque and flux [40]. Another problem discussed in the literature is the discrepancy between the actual PWM voltage and the voltage command generated by the controller. This difference can be modeled by a zero-order hold (ZOH) [41]. However, at high speeds, essential in electric vehicle applications, the ZOH effect can lead to a phase delay on the actual voltage [39], [42], [43]. MPC (Model Predictive Control) is an effective method for high-speed drive systems, particularly in traction drive applications. It predicts the optimal voltage vector by using a discrete-time model to minimize a cost function across seven voltage vectors from the inverter. However, its performance is sensitive to the choice of model and parameter variations, such as changes in stator resistance due to temperature fluctuations [44], [45]. As the FOC, MPC control technique depends on sequential motor phase current measurements and fail if a measurement element malfunctions [46]. The proportional–integral–derivative (PID) controller have a great importance in industry due to their effective balance of simplicity and performance, and it is resilient and stable across a wide range [33]. Proportional–integral (PI), kind of PID, controllers are widely used in control systems to regulate a process variable, such as the speed or position of a motor. The PI controller has two parameters: the proportional gain (Kp) and the integral gain (Ki), which determine the response of the controller [46], [47]. Indeed, setting the PI controller parameters is key for optimum motor performance. To achieve precise monitoring of the rotational speed with minimal ripple in the low-speed and high-torque operations of the five-phase machine, the PI controller is used in [48], [49]. In [50], nonlinear adjustments of the PI controller are used to achieve fast response and low overshoot, while Fractional-Order PI controllers have shown promise in PMSM drive applications [51].

A PI controller based on fuzzy logic has been employed for robust stability and rapid response times in electric vehicle powertrain control [52]. Although the advantages mentioned earlier are noteworthy, conventional PID controllers require a linear model, which cannot guarantee robustness against uncertainties due to the significant nonlinear dynamics of the PMSM motor.

This study makes two main contributions. The first is the generation of a speed profile to be followed by an autonomous electric vehicle. This profile is constructed based on the detection and classification of speed limit signs using the YOLOv10 image processing algorithm, which is recognized for its reliability under real-world traffic conditions. After the detection of each speed limit sign, the value indicated on the sign is transmitted to the control mechanism. This value serves as a speed reference that the vehicle's motor must follow. The second contribution of this study is the development of a fuzzy PI controller (Fuzzy-PI) to ensure precise tracking of this reference by the motor. The calculation of the PI controller parameters is based on two distinct approaches. The first approach reformulates the problem as an LQR (Linear Quadratic Regulator) control problem. The second approach reformulates the problem in terms of Linear Matrix Inequalities (LMI), combining the H∞ control technique with a Lyapunov function of the LILF.

The remainder of this paper is structured as follows: Section 2 describes the AV system, its overall configuration, and the methodology adopted. Section 3 presents the YOLOv10 algorithm employed for detecting and classifying traffic speed signs. Section 4 focuses on the Fuzzy T-S modeling of the PMSM. Section 5 discusses the design and development of a Fuzzy-PI controller, using both LQR and H∞ approaches, to control the PMSM under target operating conditions. Section 6 presents the results of the proposed algorithm and the control strategies. Finally, Section 7 concludes the paper.

2. Methodology

The system operates as follows: while the vehicle is in motion, an onboard camera captures real-time images of the road. These images are analyzed by an algorithm based on YOLOv10, designed to detect and recognize speed limit signs. The speed indicated on the signs is then compared to the vehicle's current speed. In case of a discrepancy, a Fuzzy-PI controller adjusts the engine inputs to automatically align the vehicle's speed with the detected speed limit. Fig. 1 illustrates the proposed control strategy.

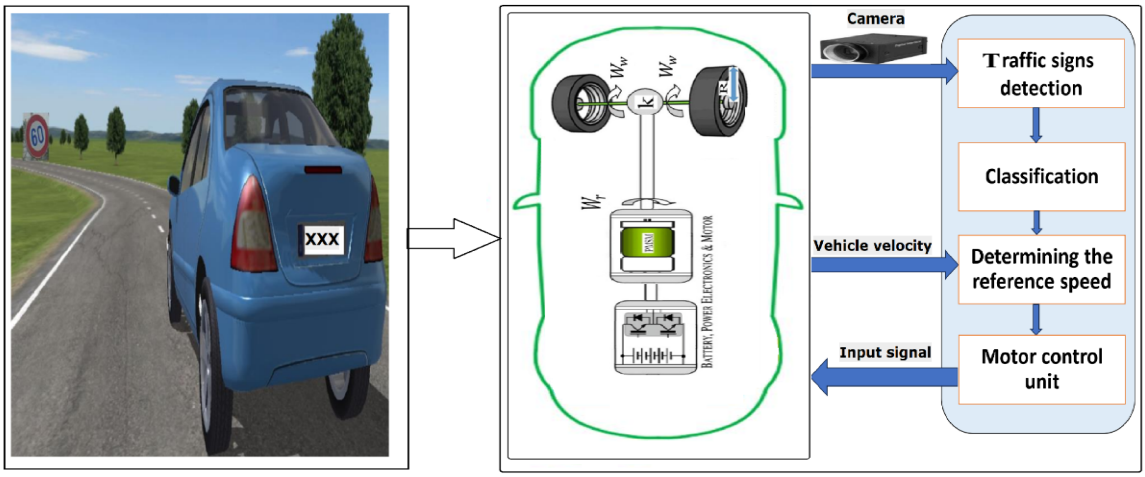

Fig. 1. The proposed control strategy method

Specifically, the parameters of the Fuzzy-PI, represented by the gain matrix $K = [K_P \ K_I]$, is determined by reformulating the control problem as an optimization task based on optimal control and the H∞ method:

- In the LQR-based approach, the gain matrix K is computed offline by solving the algebraic Riccati equation, as detailed in Corollary 1 (Section 5.1).
- In the H∞ method, the gain matrix is also computed offline, but through the solution of a set of Linear Matrix Inequalities (LMIs), as explained in Corollary 2 (Section 5.2).

Remark. The article focuses on detecting speed limit signs to adjust the vehicle's longitudinal speed. This detection allows for controlling the engine based on the displayed speed limits. Other traffic signs related to direction are not covered, as they affect steering angle rather than speed management. The main goal is to ensure the vehicle follows the reference speed set by these signs.

3. Object Detection

Convolutional Neural Networks (CNNs) are models particularly effective for processing spatially structured data, such as images. Unlike Multilayer Perceptron (MLPs), which use fully connected layers, CNNs use convolutional layers to extract local features from images. Each convolutional layer performs a convolution operation, enabling the detection of specific patterns in the image. While many popular CNNs end with fully connected layers, convolution remains central to their function. YOLO (You Look Only Once) is an algorithm based on deep neural networks with real-time object detection capabilities. This state-of-the-art technology is widely available, mainly due to its speed and precision.

Its quick and accurate detection has enabled YOLO to become one of the most commonly utilized approaches in computer vision. Here, the traffic sign provides a visual guide to communicate road conditions, potential hazards, and other pertinent details for safe navigation on the road [53]. YOLO, meanwhile, is a convolutional neural network-based object detection algorithm that has been specifically designed [54]. The algorithm has been selected based on its competitiveness with other

DL-based methods with regard to processing speed on GPUs, high performance with respect to relevant measures, and simple architecture [55]–[57].

3.1. YOLOv10 Model

The YOLOv10 model, representing the latest step forward in the line of the YOLO series, proposes an improved architecture facilitating better detection capabilities. The architecture of YOLOv10, as shown in Fig. 2, consists of a structured combination of backbone, neck, and head modules.

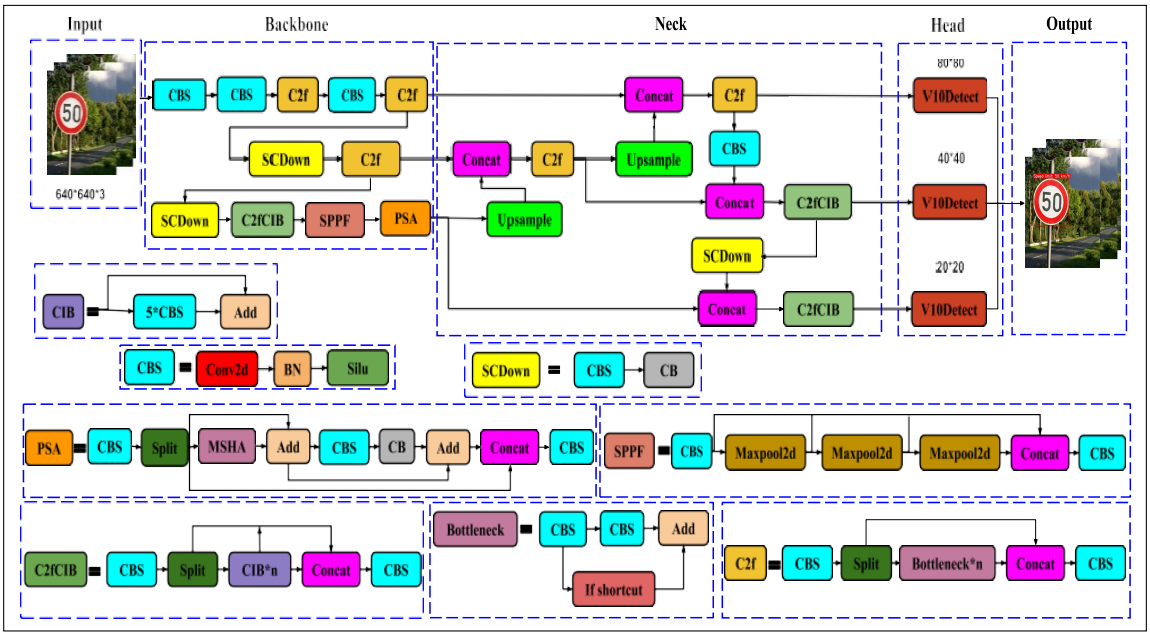

Fig. 2. YOLOv10 architecture: Backbone, neck, and head components for object detection

The backbone uses layers such as Convolution-BatchNorm-Silu (CBS) and Pyramid Spatial Attention (PSA) modules to extract salient features from input images, while the neck fuses multi-scale features into one through up sampling and concatenation to enhance detection of objects of different sizes. The head then produces the detection output at three scales, optimizing object detection for both small objects and those with more complex appearances. YOLOv10 offers several variants, each designed to balance speed and accuracy to suit various use cases. Table 1 provides a performance comparison across these YOLOv10 models, ranging from the lightweight YOLOv10-N to the high performance YOLOv10-X.

Table 1. Performance comparison of YOLOv10 model variants across different metrics

Model	Test Size	Params	FLOPs	APval	Latency
YOLOv10-N	640	2.3 M	6.7 G	38.5 %	1.84 ms
YOLOv10-S	640	7.2 M	21.6 G	46.3 %	2.49 ms
YOLOv10-M	640	15.4 M	59.1 G	51.1 %	4.74 ms
YOLOv10-B	640	19.1 M	52.5 G	52.5 %	5.74 ms
YOLOv10-L	640	24.4 M	53.2 G	53.2 %	7.28 ms
YOLOv10-X	640	29.5 M	54.4 G	54.4 %	10.70 ms

Each variant comes with its own distinct concoction of parameters and computational requirements, measured in FLOPs, which essentially indicate the total number of operations (multiplications, additions, etc.) that a model performs for a single inference pass. Another parameter that reflects some performance indexes is APval (the Average Precision on the Validation set), which balances precision and recall of the model against the unseen validation data evaluation. For instance, YOLOv10-N accomplishes 38.5% APval performance with low latency, featuring a mere 2.3 million

parameters and 6.7 GFLOPs (Billion Floating Point Operations) or rather, billions of operations, best suited for real-time applications on hardware with scarce resources. Conversely, the most powerful variant, YOLOv10-X, achieves an APval of 54.4% and has a latency of 10.70 ms, making it well-suited for scenarios demanding very high precision. The different configurations highly depict the vocal adaptability of YOLOv10 as an effective facilitator for meeting varying object detection requirements ranging from ultra-fast executions to super accurate detections.

3.2. Dataset

For training and validation of YOLOv10 model, the traffic sign detection model used data gathered from multiple sources. We captured photos in real world street environments and also collected images from online sources, using databases and search engines such as IPM Images, Google, and Bing. All images were then standardized to a resolution of 640×640 pixels for consistency. Fig. 3 shows a sample of this data.

Fig. 3. Validation sample images used for training and validation of the speed limit traffic sign detection model

The image preprocessing stage for training deep learning models highlighted the critical role of image annotation. This process involves extracting key features from images and assigning appropriate labels based on predefined inputs, providing the labeled data essential for supervised learning tasks. In this study, the Makesense online platform was used for image annotation, as shown in Fig. 4, streamlining the process and enhancing labeling accuracy, thereby improving the overall quality and effectiveness of the training dataset for the deep learning model.

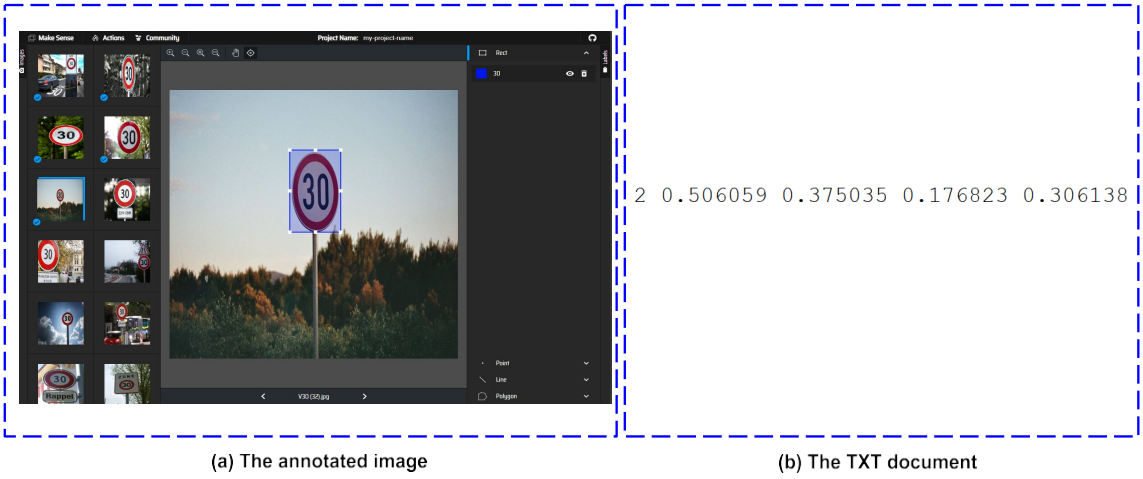

Fig. 4. Image annotation in the Makesense platform

Additionally, the datasets were divided into training and validation sets with an 80:20 ratio (80% for training and 20% for validation), as outlined in Table 2.

Table 2. Data for traffic signs detection model

Speed Limit / Data	Stop	20 km/h	30 km/h	40 km/h	50 km/h	60 km/h	70 km/h	80 km/h	90 km/h	100 km/h	120 km/h
Train	80	72	88	84	65	100	71	98	107	66	60
Validation	21	18	23	22	17	25	18	25	27	17	16
Total	101	90	111	106	82	125	89	123	134	83	76

4. Motor Modeling and Control

The main difference between an internal combustion engine vehicle (ICEV) and an electric vehicle (EV) lies in the type of motor used, which varies depending on the energy source. Indeed, ICEVs run on fuel, while EVs are powered by electric batteries. However, the motor plays a crucial role in converting energy in EVs. This process takes place directly within the motor, an electric machine that transforms electrical energy into mechanical energy, with an intermediate phase that uses magnetic energy. This phase generates a rotating magnetic field, typical of alternating current machines. Fig. 5 shows the main powertrain components of an EV.

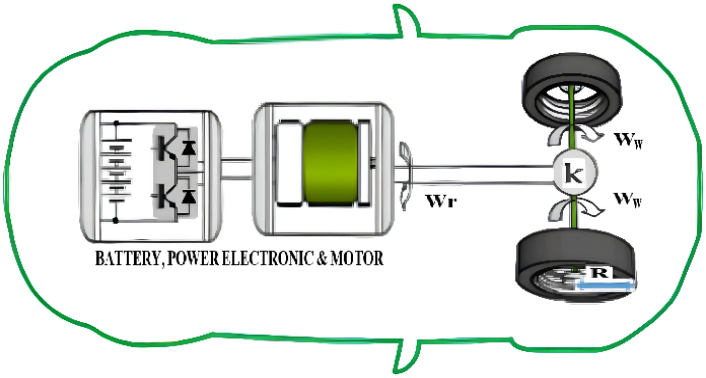

Fig. 5. The electric vehicle drive train

According to the fundamental principle of dynamics, the following formulas apply:

$$m\frac{dVx}{dt} = -F_x \tag{1a}$$

$$J_v \frac{dW_w}{dt} = -T_b + rF_x \tag{1b}$$

Where m, W_w and J_v denote respectively the vehicle mass, the wheel angular velocity and the inertia of the vehicle, while V_x is the longitudinal velocity of the vehicle, T_b is braking torque and F_x denotes the longitudinal friction force. It's obvious that the force F_x is a natural by-product of the torque generated by the electric motor.

The (1a) and (1b) leads to the following relationship between the vehicle's longitudinal velocity and the motor's angular velocity:

$$m\frac{dV_x}{dt} = -\frac{J_v}{r}\frac{dW_w}{dt} - \frac{1}{r}T_b \tag{2}$$

This equation illustrates that the motor is the source of longitudinal control for the EV. However, different types of electric motors are used in electric vehicles EVs, and their performance largely depends on the control strategy implemented.

4.1. Overview of Propulsion Machines in EVs

The performance of electric vehicles directly results from the performance of the motor, which is determined by the torque-speed and power-speed characteristics of the traction motor as shown in Fig. 6.

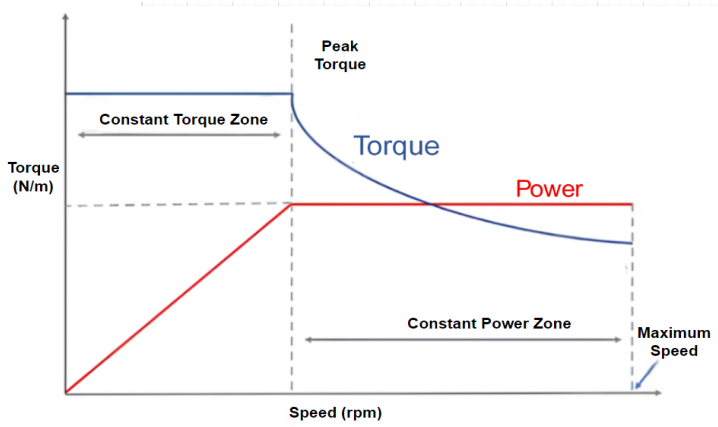

Fig. 6. Torque-speed and power-speed characteristics of the traction motor [58]

At low speeds, it is crucial to ensure smooth acceleration and good climbing performance, which requires maximum and constant torque. The maximum speed is determined by the constant power zone, where torque is minimal [58]. Therefore, to achieve optimal performance from an electric vehicle motor, it is essential to find a balance between acceleration capabilities and a wide range of speeds within this constant power zone. Against this backdrop, different types of motors are used in electric vehicles, such as brushed direct current (DC) motors, brushless direct current (BLDC) motors, synchronous reluctance motors (SynRM), switched reluctance motors (SRM), induction motors (IM), and permanent magnet synchronous motors (PMSM). Table 3 summarizes the main selection criteria for a motor in electric propulsion applications.

Table 3. Electric motor criteria

Factors / Moteur	Cost	Size	Efficiency	Fault tolerance	Overload capacity	Power density	Speed range	Torque ripple	Control simplicity	Noise level
BLDC	✓✓✓✓	✓✓✓	✓✓✓	✓✓	✓✓✓	✓✓	✓✓	✓✓✓✓✓	✓✓✓✓	✓✓✓✓
SynRM	✓✓✓	✓✓✓	✓✓✓✓	✓✓✓✓✓	✓✓✓	✓✓✓✓	✓✓✓	✓✓✓✓	✓✓✓	✓✓✓✓
SRM	✓✓✓✓	✓✓	✓✓✓✓	✓✓✓✓✓	✓✓	✓✓✓	✓✓✓✓	✓✓	✓✓✓	✓✓
IM	✓✓✓✓✓	✓✓✓✓	✓✓✓	✓✓✓	✓✓✓✓	✓✓✓	✓✓	✓✓✓✓✓	✓✓✓✓	✓✓✓✓
PMSM	✓✓✓	✓✓✓✓✓	✓✓✓✓✓	✓✓✓✓	✓✓✓	✓✓✓✓✓	✓✓	✓✓✓✓	✓✓✓✓	✓✓✓✓

These include efficiency, maximum torque, size, speed range, cost, power density, technical maturity, reliability, and [59]–[61]. These motors have been examined and compared. To properly rank these motors, a score is assigned to each criterion, ranging from one check (✓), which corresponds to a very low rating, to five checks (✓✓✓✓✓), which corresponds to a very high rating.

Therefore, according to Table 3, due to their excellent efficiency, higher torque, and established production and control procedures, PMSMs have an edge over their competitors and are the most common type of electric motor used in EVs [61]–[63]. This is clearly demonstrated in Table 4 below, which presents the different manufacturers of commercial electric vehicles in chronological order [58].

Table 4. Commercial electric vehicle historical database.

Motor Type (Abbreviation)	Estimated Market Share Worldwide	Example Vehicle Brands
Permanent Magnet Synchronous AC Motors (PMSM)	40 - 50%	Tesla, Audi, Hyundai, Allez, Volkswagen, Mercedes-Benz, Gué, Porsche, Volvo, MG…
Variable Reluctance AC Motors (VRM)	10% - 20%	Nissan, MONDE
Brushed DC Motors/Permanent Magnet Synchronous Motors (DCB/PMSM)	5% - 10%	Renault
Brushless DC Motors (BLDC)	20- 30%	BMW
Synchronous Reluctance Motors (SRM)	5% - 10%	Chevrolet
Permanent Magnet Synchronous AC Motors/Brushless DC Motors (PMSM/BLDC)	-	Jaguar

In 2025, 60 to 70% of electric vehicles will use PMSM motors. Well-known companies such as Porsche, Hyundai, and BMW have been using PMSM motors for over a decade. Tesla, which only used induction motors until 2015-2016 [64], has recently shifted towards using PMSM motors in models such as the Model 3 and Model Y. Although Audi and Mercedes have traditionally opted for induction motors [65], [66]. They are beginning to shift towards the use of PMSM motors in certain models. For example, Audi offers models such as the Audi e-tron GT and Audi RS e-tron GT equipped with PMSM motors, while Mercedes has developed models like the Mercedes EQC, Mercedes EQS, and Mercedes EQB. These reasons encourage us to take an interest in the control of this type of engine in this work.

4.2. PMSM Motor Modeling

The purpose of this subsection is to describe the dynamics of the PMSM. The expression for the d-q components of the voltage circulating in the stator of the PMSM machine can be described as follows [62]:

$$\begin{cases} V_q = R_s i_q + L_q \dfrac{di_q}{dt} + W_r L_d i_d + W_r \phi_m \\ V_d = R_s i_d + L_d \dfrac{di_d}{dt} - W_r L_q i_q \end{cases} \tag{3}$$

Where V_q , V_d are dq-fram voltage, $i_q$and i_d are dq-frame currents, R_s is winding resistance, L_q, L_d are dq-frame inductance's, ϕ_m is flux linkage established by PMSM and W_r is electrical rotor rotation speed. Moreover, using the fundamental principle of dynamics, the mechanical equation governing the operation of the PMSM can be written as follows:

$$\frac{dW_r}{dt} = \frac{-B}{J} W_r + \frac{3{n_p}^3 \phi_m}{8J} i_q - \frac{n_p C_r}{2J} \tag{4}$$

Where J denotes the inertia of the motor. The electromagnetic torque C_e generated by PMSM motor is given by:

$$Ce = \frac{2J}{n_p} \frac{dW_r}{dt} + \frac{2B}{n_p} W_r + C_r \tag{5}$$

Where B is the damping coefficient, J is the inertia coefficient, n_p is the number of magnetic poles and C_r is the load torque. Moreover, Ce can be written as [62]:

$$Ce = \frac{3\, n_p}{4} [\phi_m i_q + (L_q - L_d) i_q i_d] \tag{6}$$

In a PMSM motor with surface-mounted magnets (where $L_q \approx L_d$), this leads to:

$$Ce = \frac{3\,n_p}{4}\phi_m i_q \tag{7}$$

4.3. Takagi-Sugeno Fuzzy Modeling

Consider a nonlinear system represented by:

$$\dot{x} - f(x,u) = 0 \tag{8}$$

Using the T-S fuzzy representation [67], this system can be expressed as follows:

$$\dot{x}\,(t) = \sum_{i=1}^{r} h_i(\theta(t))[A_i\,x(t)\; + B_i u(t)] \tag{9}$$

Where the remise variable $\theta(t)$, is bounded by a maximum and minimum value $\theta^{min} \leq \theta(t) \leq \theta^{max}$, which allows it to be written as follows:

$$\theta(t)\; = \lambda_1\big(\theta(t)\big)\,\theta^{min} + \lambda_2(\theta)\,\theta^{max} \tag{10}$$

$\lambda_1(\theta(t))$ and $\lambda_2(\theta(t))$ are defined as follows:

$$\begin{cases} \lambda_1(\theta(t)) \;=\; \dfrac{\theta^{max} - \theta(t)}{\theta^{max} - \theta^{min}} \\ \lambda_2(\theta(t)) \;=\; \dfrac{\theta(t) - \theta^{min}}{\theta^{max} - \theta^{min}} \end{cases} \tag{1a}$$

Where $\sum_{i=1}^{2} \lambda_i(\theta(t)) = 1$ and $0 \leq \lambda_i(\theta(t) \leq 1$, $i = 1{,}2$. The weighting functions $h_i(\theta(t))$ represented as follows:

$$h_i(\theta(t)) \;= \frac{\lambda_i(\theta(t)}{\sum_{i=1}^{r} \lambda_i(\theta(t)} \tag{12}$$

And satisfy the following convexity conditions:

$$\sum_{i=1}^{r} h_i\big(\theta(t)\big) = 1 \; and \; 0 \leq h_i(\theta(t) \leq 1, \;\; i = 1, r \tag{13}$$

The T-S fuzzy representation is well known for dealing with nonlinearities arising from complex systems such as the PMSM model [62], [68].

5. Control Strategy

The main objective of this section is to develop a control strategy that enables the vehicle to track a desired longitudinal reference speed profile, denoted as $V_x{}^d$, detected by the YOLOv10 algorithm. It is known that the longitudinal speed of a vehicle, denoted as Vx, is a function of the rotational speed of its engine, denoted as W_r. Under certain driving conditions, the longitudinal speed can be considered proportional to the engine's rotational speed. This proportional relationship is valid under specific assumptions, including the presence of a direct transmission or a constant gear ratio (as is often the case with automatic gearboxes), a wheel slip value $\leqslant 0.2$, an engine operating steadily within its optimal range of revolutions per minute, and negligible mechanical and aerodynamic losses. In such conditions, the vehicle's speed is directly influenced by the engine speed, the transmission ratio, and the radius of the wheels. The relationship between the vehicle's longitudinal speed and the engine's rotational speed can be expressed as $Vx = K \cdot W_r$, where $K = R \cdot k$, R is the wheel radius, and

k is the overall gear ratio. The key idea is to regulate the engine, represented by PMSM, so that it rotates with an angular speed ${W_r}^d$, which corresponds to the reference speed ${V_x}^d$.

The structure of the proposed fuzzy controller is shown in Fig. 7 and is given as follows:

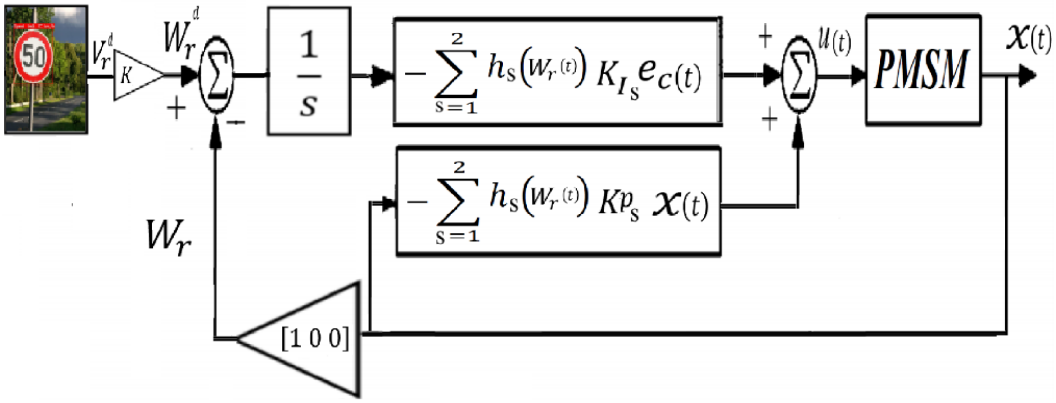

Fig. 7. Structure of the proposed fuzzy controller strategy

$$u(t) = -\sum_{s=1}^{2} h_s(W_r(t)) \left[K_{ps} x(t) + K_{Is} \int_0^t (W_r - {W_r}^d) dt \right] \tag{14}$$

The LQR and H∞ approaches are used to calculate the parameters of the proposed Fuzzy-PI controller (14).

5.1. LQR Approach

This subsection aims to develop the controller (14) for our PMSM system using LQR control. This method is used to design an optimal controller for linear systems, aiming to minimize a cost defined by an objective function. In our case, since the system is nonlinear, we first aim to bypass the nonlinearity issue by using the T-S fuzzy representation. This approach allows the system to be modeled as local linear subsystems, as explained in the previous section. Then, we seek to compute the optimal sub-controller K_s for each local subsystem using the LQR control approach. Finally, the global controller will be the sum of the sub-controllers K_s, weighted by membership functions, as follows:

$$K = \sum_{s=1}^{2} h_s K_s \tag{15}$$

Where $K_s = [K_{Ps} \;\; K_{Is}]$ and h_s, $s = 1,2$. satisfy the convexity conditions (13). Note that the controller development carried out in this section assumes that the disturbance term Cr (due to the effect of load torque) is neglected in (5).

Let e_c represent the integral error between the desired and actual angular rotational speeds:

$$e_c = \int W_r - {W_r}^d \tag{16}$$

Consider the $W_r(t)$ remise variable, ${W_r}^{min} \leq W_r(t) \leq {W_r}^{max}$, By combining (3), (4), (7) and (14), and according to the T-S fuzzy representation (9), where ($\theta(t) = W_r(t)$), the PMSM model can be expressed as follows:

$$\dot{x}\,(t) = \sum_{i=1}^{2} h_i(W_r(t))[A_i\,x(t) + B_i u(t)] = g(x,u) = 0 \tag{17}$$

Where, $h_i(W_r(t)$ satisfies (13) and

$$x = [W_r \quad i_q \quad i_q \quad e_c]^T \text{ and } u = [V_q \quad V_q]^T$$

$$A_1 = \begin{bmatrix} \frac{-B}{J} & \frac{3{n_p}^3\phi_m}{8J} & 0 & 0 \\ \frac{-\phi_m}{L_q} & \frac{-R_s}{L_q} & \frac{-L_d}{L_q}{W_r}^{min} & 0 \\ 0 & \frac{-L_q}{L_d}{W_r}^{min} & \frac{-R_s}{L_d} & 0 \\ 0 & 0 & 0 & 1 \end{bmatrix}$$

$$A_2 = \begin{bmatrix} \frac{-B}{J} & \frac{3{n_p}^3\phi_m}{8J} & 0 & 0 \\ \frac{-\phi_m}{L_q} & \frac{-R_s}{L_q} & \frac{-L_d}{L_q}{W_r}^{max} & 0 \\ 0 & \frac{-L_q}{L_d}{W_r}^{max} & \frac{-R_s}{L_d} & 0 \\ 0 & 0 & 0 & 1 \end{bmatrix}$$

$$B_i = B = \begin{bmatrix} 0 & 0 \\ \frac{1}{L_q} & 0 \\ 0 & \frac{1}{L_d} \\ 0 & 0 \end{bmatrix}$$

Let the following cost function $J(x,u)$ be as:

$$J = \frac{1}{2}\int_0^{\infty} [x^T(t)\,Qx(t) + u^T(t)\,Ru(t)]dt \tag{18}$$

Where $Q \geq 0$ and $R > 0$ are the weighting matrices of $x(t)$ and $u(t)$.

Corollary 1. The optimal sub-controller K_i for each local subsystem i, can be obtained as $K_i = R^{-1}{B_i}^T P$, where $P > 0$ is the solution of the following equation:

$${A_i}^T P + P\,A_i - PR^{-1}{B_i}^T P + Q = 0 \qquad i = 1,2. \tag{19}$$

The lqr function in MATLAB's Control System Toolbox easily solves the linear optimal control problem by computing the solution to (19). This equation is derived from the proof below.

Proof 1: The approach presented in this section is based on the definition of the Hamiltonian of a system. Indeed, the Hamiltonian allows modeling the system's evolution by incorporating both the cost function and the constraints that must be satisfied during its evolution.

$$H(x,\rho) = \frac{1}{2}[x^T(t)\,Qx(t) + u^T(t)\,Ru(t)] + \rho^T\,g(x,u) \tag{20}$$

Given (17), this Hamiltonian can be expressed as:

$$H(x,\rho) = \frac{1}{2}[x^T(t)\,Qx(t) + u^T(t)\,Ru(t)] + \rho^T \sum_{i=1}^{2} h_i(W_r(t))[A_i\,x(t) + B_i u(t)]$$
$$H(x,\rho) = \sum_{i=1}^{2} h_i(W_r(t)\,H_i(x,\rho) \quad (21)$$

Where $\rho(t)$ are the Lagrange multipliers, auxiliary variables that account for the constraints imposed on the system's state evolution, such as its dynamics. These variables are crucial in the demonstration of the optimal control approach. They are also referred to as the system's adjoint state vector and are related to the state variables by the following linear equation:

$$\rho\,(t) = Px(t) \quad (22)$$

The Pontryagin maximum principle consists of minimizing the system's Hamiltonian with respect to its input $u(t)$:

$$\frac{\partial H_i(x,\rho)}{\partial u(t)} = 0 \;\; = Ru(t) + B_i{}^T\rho(t) \quad (23)$$

From (23), $u(t)$ can be expressed as follows:

$$u(t) = -R^{-1}B_i{}^T\rho \quad (24)$$

By combining (24), (22), and (17):

$$\dot{x}\,(t) = \sum_{i=1}^{2} h_i \;\; [A_i\,x(t) - B_i R^{-1}B_i{}^T Px(t)] \quad (25)$$

A state-feedback control law is currently being identified as:

$$u(t) = K_s\,x(t) \quad (26)$$

Where:

$$K_s = -\,R^{-1}B_i{}^T P \quad (27)$$

The Lagrange multipliers $\rho(t)$ follow a differential equation, called the adjoint equation:

$$\frac{d\rho\,(t)}{d\,t} = -\frac{\partial H_i}{\partial x(t)} = -(Qx(t) + A_i{}^T\,\rho\,(t)) \quad (28)$$

The derivation of (22) leads to:

$$\dot{\rho}(t) = P\dot{x}(t) \quad (29)$$

By substituting (25) into (29) and equating the result to (28):

$$-(Qx(t) + A_i{}^T\,P(t)x(t)) = P(t)\,A_i\,x(t) - P(t)R^{-1}B_i{}^T P(t)x(t) \quad (30)$$

Finally, we find:

$$A_i{}^T\,P + P\,A_i - PR^{-1}B_i{}^T P + Q = 0 \qquad i = 1{,}2 \quad (31)$$

5.2. H∞ Controller

Let $x = [W_r \quad i_q \quad i_q]^T$, from (3), (4), (7) and (14) the following state-space representation can be formulated:

$$\begin{bmatrix} \dot{W_r} \\ \dot{i_q} \\ \dot{i_d} \end{bmatrix} = \begin{bmatrix} \frac{-B}{J} & \frac{3{n_p}^3\phi_m}{8J} & 0 \\ \frac{-\phi_m}{L_q} & \frac{-R_s}{L_q} & \frac{-L_d}{L_q}W_r \\ 0 & \frac{-L_q}{L_d}W_r & \frac{-R_s}{L_d} \end{bmatrix} \begin{bmatrix} W_r \\ i_q \\ i_d \end{bmatrix} + \begin{bmatrix} 0 & 0 \\ \frac{1}{L_q} & 0 \\ 0 & \frac{1}{L_d} \end{bmatrix} \begin{bmatrix} V_q \\ V_d \end{bmatrix} + \begin{bmatrix} \frac{-n_p\, Cr}{2J} \\ 0 \\ 0 \end{bmatrix} \tag{32}$$

In compact form, (32) can be represented as:

$$\begin{cases} \dot{x}\,(t) = f(x(t), u(t)) + v(t) \\ y(t) = \ W_r = [1\ 0\ 0]x(t) = C\ x(t) \end{cases} \tag{33}$$

Where $v(t)$ are distrubances of the system that can be represented by:

$$v(t) = \begin{bmatrix} \frac{-n_p}{2J} \\ 0 \\ 0 \end{bmatrix} = \begin{bmatrix} \frac{-n_p}{2J} & 0 & 0 \\ 0 & 0 & 0 \\ 0 & 0 & 0 \end{bmatrix} \begin{bmatrix} Cr \\ 0 \\ 0 \end{bmatrix} = D\Psi(t) \tag{34}$$

According to the T-S fuzzy representation (9), where $W_r(t)$ remise variable ($\theta(t) = W_r(t)$), the system (33) can be represented as follows:

$$\begin{cases} \dot{x}\,(t) = \sum_{i=1}^{2} h_i(W_r(t))[A_i\,x(t) + B_i u(t) + D_i\Psi(t)] \\ y(t) = \sum_{i=1}^{2} h_i(W_r(t))C_i\,x(t) \end{cases} \tag{35}$$

Where

$$A_1 = \begin{bmatrix} \frac{-B}{J} & \frac{3{n_p}^3\phi_m}{8J} & 0 \\ \frac{-\phi_m}{L_q} & \frac{-R_s}{L_q} & \frac{-L_d}{L_q}{W_r}^{min} \\ 0 & \frac{-L_q}{L_d}{W_r}^{min} & \frac{-R_s}{L_d} \end{bmatrix};\ A_2 = \begin{bmatrix} \frac{-B}{J} & \frac{3{n_p}^3\phi_m}{8J} & 0 \\ \frac{-\phi_m}{L_q} & \frac{-R_s}{L_q} & \frac{-L_d}{L_q}{W_r}^{max} \\ 0 & \frac{-L_q}{L_d}{W_r}^{max} & \frac{-R_s}{L_d} \end{bmatrix}; B = \begin{bmatrix} 0 & 0 \\ \frac{1}{L_q} & 0 \\ 0 & \frac{1}{L_d} \end{bmatrix}$$

$$B_i = B \ \ and \ \ D_i = D$$

5.2.1. Some Mathematical Lemmas

Lemma 1. [69]; Let X and Y denote two matrices with appropriate dimensions.

$$X^TY + Y^TX \ \leq {}_\gamma{}^{-1}X^TX + {}_\gamma Y^TY \tag{36}$$

Lemma 2. [70]; Consider a matrix Z_{isj} of appropriate dimensions, where $\{i, s, j\} = 1 \ldots r$. Under these conditions, the following inequality holds: if $Z_{isj} < 0$, then

$$\sum_{i=1}^{r}\sum_{s=1}^{r}\sum_{j=1}^{r} Z_{isj} < 0 \tag{37}$$

Lemma 3. [62]; Let Q, R and S be matrices of appropriate dimensions with $Q = Q^T$ and $R = R^T$, The following expressions hold:

$$\begin{bmatrix} Q & S \\ * & R \end{bmatrix} < 0 \Leftrightarrow \begin{cases} R < 0 \\ Q - S^T R^{-1} S < 0 \end{cases} \tag{38}$$

5.2.2. Stability Analysis Using Line Integral Lyapunov Function (LILF)

Typically, the Lyapunov quadratic (QLF) approach is employed to achieve stability analysis and stabilization for Takagi–Sugeno fuzzy models derived from linear or bilinear matrix inequality conditions. The (QLF) function involving finding a common matrix $P = P^T > 0$ that satisfies the constraints for each subsystem of the fuzzy set, which can be a very hard task and can lead to a conservative and time-consuming solution [71], [72]. The (LILF) function is defined as the integral of a scalar function along a trajectory of the system [73]. This technique is based on the analysis of the local stability for each system and, subsequently, the global function will be a fuzzy intersection between all these local functions [74], which leads to less restrictive stability conditions.

Consider the following LILF function:

$$V(x(t)) = 2 \oint_{\Gamma(0;x)} f(\phi) d\phi \tag{39}$$

Rhee et al. [73] demonstrate that (39) is a Lyapunov Function if the following condition is verified

$$\frac{\partial f_m(x)}{\partial x_n} = \frac{\partial f_n(x)}{\partial x_m}; \quad for\ n \neq m, \{n, m\} = \{1, 2 \dots n\} \tag{40}$$

Where $f(x(t)) = \sum_{i=1}^{r} h_i(\Theta) H_i x(t) > 0$; function of $x(t)$, $H_i x(t) = (H0 + \sum_{i=1}^{r} h_j(\Theta)) D_i) x(t)$.

The diagonal elements are different according to the fuzzy sets in the premise parts of the fuzzy rules [73].

$$H0 = H0^T = \begin{bmatrix} 0 & h_{12} & h_{12} & \dots & h_{1n} \\ * & 0 & h_{23} & \dots & h_{2n} \\ * & * & \ddots & & \vdots \\ * & * & \dots & 0 & \end{bmatrix}; \quad D_i = \begin{bmatrix} {d_{11}}^i & 0 & 0 & \dots & 0 \\ * & {d_{22}}^i & 0 & \dots & 0 \\ * & * & \ddots & & \vdots \\ * & * & \dots & {d_{nn}}^i & \end{bmatrix}$$

The Analysis Based on Quadratic Lyapunov Function (QLF) can therefore be considered as a special form of Line Integral Lyapunov Function (LILF) [73].

Let's consider the H∞ performance related to the tracking error $e_c(t)$:

$$\int_0^\infty {e_c}^T(t)\, e_c(t) dt \leq \gamma^2 \int_0^\infty \xi^T(t)\, \xi(t)\, dt \tag{41}$$

In order to design the controller (14) for the closed-loop T-S fuzzy model system (35), the Lyapunov function (39) and H∞ approach (41) will be used. The controller gains will be derived by solving the LIMs conditions presented in Corollary 2.

Corollary 2. If there are symmetric positive definite matrices $X_j, Y_{sj}, K_s,$ and scalars $\gamma > 0$, can satisfy the following inequalities:

$$\begin{bmatrix} \Xi_{isj} & \widehat{D} & XM^T \\ * & -\gamma I & 0 \\ * & * & -I \end{bmatrix} < 0$$

Where:

$$\Xi_{isj} = \widehat{A}_\iota X_j + X_j \widehat{A}_\iota^T - \widehat{B}_\iota Y_{sj} - Y_{sj}{}^T \widehat{B}_\iota^T \; ; \; Y_{sj} = K_s X_j \tag{42}$$

Then the system (35) is stable asymptotically and the H_∞performances (41) are guaranteed with attenuation level γ^2.

Where X_j and Y_{sj} (thus $Ks = Y_{sj} X_j{}^{-1}$) can be easily obtained by solving (42).

Proof 2: Let's denote $\hat{x} = \begin{bmatrix} x \\ e_c \end{bmatrix}$ the augmented state, from (35) and (16) the following augmented system is obtained:

$$\dot{\hat{x}}(t) = \sum_{i=1}^{2} \sum_{s=1}^{2} h_i h_s \left[\left(\widehat{A}_\iota - \hat{B} K_s \right) x + \widehat{D} \xi(t) \right] \tag{43}$$

Where:

$$\widehat{A}_\iota = \begin{bmatrix} A_i & 0 \\ M & 0 \end{bmatrix}; \hat{B} = \begin{bmatrix} B \\ 0 \end{bmatrix}; \; \widehat{D} = \begin{bmatrix} A_i & D \\ 0 & 0 \end{bmatrix};$$

$$M = [1\ 0\ 0]; \; K_s = \begin{bmatrix} K_{ps} \; K_{Is} \end{bmatrix}; \; \xi(t) = \begin{bmatrix} W_r{}^d \\ \Psi \end{bmatrix}$$

To achieve these goals, the H_∞ performance related to the tracking error e_c (41), combined with the derivative of (39), is considered:

$$\dot{V}(x(t)) + e_c{}^T(t) \, e_c(t) - \gamma^2 \xi(t)^T \xi(t) < 0 \tag{44}$$

This inequality leads to the following expression by incorporating the T-S fuzzy model structure:

$$\sum_{i=1} \sum_{s=1} \sum_{j=1} h_i h_s h_j \dot{\hat{x}}(t)^T P_j \hat{x}(t) + \hat{x}(t) \, P_j \dot{\hat{x}}(t) + \hat{x}^t(t) \, M^T M \, \hat{x}(t) - \gamma^2 \xi(t)^T \xi(t) < 0 \tag{45}$$

In the rest of this demonstration, to simplify writing, we adopt the following notation:

$$\sum_{i=1} \sum_{s=1} \sum_{j=1} h_i h_s h_j = \sum_{i,s,j=1} h_{isj}$$

Substituting the expression of $\dot{\hat{x}}(t)$ in (43), (45) become:

$$\begin{aligned} \sum_{i,s,j=1} h_{isj} \left[\left[\left(\widehat{A}_\iota - \hat{B} K_s \right) + \widehat{D} \xi(t) \right]^T P_j \hat{x}(t) + \hat{x}(t) \, P_j \left[\left(\widehat{A}_\iota - \hat{B} K_s \right) x + \widehat{D} \xi(t) \right] \right. \\ \left. + \hat{x}^t(t) \, M^T M \, \hat{x}(t) - \gamma^2 \xi(t)^T \xi(t) \right] < 0 \end{aligned} \tag{46}$$

By applying **Lemma 1**, (46) can be expressed as follows:

$$\sum_{i,s,j=1} h_{isj} \hat{x}(t)^T \left[\left(\widehat{A}_\iota - \hat{B} K_s \right)^T P_j + P_j \left(\widehat{A}_\iota - \hat{B} K_s \right) + \gamma^2 P_j \widehat{D}^T \widehat{D} P_j + M^T M \right] \hat{x}(t) < 0 \tag{47}$$

Post-and pre-multiply X_j, (where $X_j = P_j{}^{-1}$ and $Y_{sj} = Ks X_j$), the inequality (47) can be expressed as:

$$\widehat{A}_i X_j + X_j \widehat{A}_i^T - \widehat{B}_i Y_{sj} - Y_{sj}^T \widehat{B}_i^T + \gamma^2 \widehat{D}^T \widehat{D} + X_j M^T M X_j < 0 \; ; \{i,s,j\} = \{1,2\} \quad (48)$$

Using Schur's complement, lemma.3, LMI conditions (42) are obtained.

6. Simulations, Results and Discussion

6.1. Simulation Framework for Self-Driving Car Systems

The primary goal of this experiment is to simulate the operational workflow of self-driving cars by integrating object detection and control mechanisms. The detection model is implemented using Visual Studio Code, where it processes images from a designated data folder to identify speed signals. In this setup, detected speed values are stored in a JSON file, and corresponding images with detected signals are saved in the separate detect folder. Simultaneously, the last perceived speed in the JSON file is read by MATLAB Simulink to perform control tasks, mimicking real-time decision-making procedures in autonomous vehicles. This setup demonstrates the seamless interaction between advanced detection algorithms and control systems, underscoring their importance in developing reliable self-driving technologies. Fig. 8 illustrates the experimental setup, showing the integration of the YOLOv10 detection model, Visual Studio Code, and MATLAB Simulink to create a comprehensive simulation framework for self-driving cars.

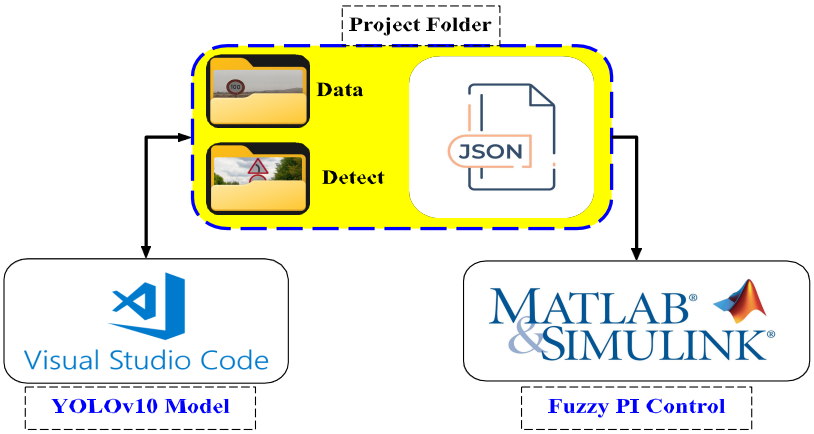

Fig. 8. Integration of YOLOv10 detection model with MATLAB Simulink for autonomous vehicle simulation

6.2. Training Environment and Evaluation Indexes

A crucial step in the training process was the completion of the labeling phase for both the training and validation datasets, ensuring accurate annotations for traffic signs. The YOLOv10-S model, selected for its balanced performance in speed and accuracy, was then trained using Google Colab. Training was conducted on an NVIDIA Tesla T4 GPU with 16 GB memory, supported by CUDA version 12.2 and driver version 535.104.05. During training, images were resized to a standard 640*640 resolution to optimize processing. Class information, including class names and total count, was recorded in a data.yaml file for easy reference across training and validation sets, with the dataset split into 80% for training and 20% for validation. The training was conducted over 300 epochs for the model to learn the critical features of traffic signs in an appropriate manner.

The performance of the model, YOLOv10-S, was examined with the help of a collection of comprehensive metrics. These metrics included precision, recall, mean average precision on the validation set (mAPval) at an Intersection over Union (IoU) threshold of 0.5, and mAPval across IoU thresholds from 0.5 to 0.95. The detection processing time was also recorded in order to measure the efficiency of the model, which is required for real-time traffic board detection applications. This assessment serves to guarantee that the YOLOv10-S model is capable of delivering accurate and timely detection outcomes during practical deployments. Precision is about the positive predictions'

accuracy, calculated as the ratio of correctly predicted positive samples to the number of all samples predicted to be positive. The formula for precision is as follows:

$$Precision = \frac{TP}{TP + FP} \tag{50}$$

Recall, on the other hand, assesses the rate of correct predictions for all actual target instances, and its formula is as follows:

$$Recall = \frac{TP}{TP + FN} \tag{51}$$

Where

- TP (True Positives): The number of positive examples correctly identified;
- FP (False Positives): The number of negative examples incorrectly classified as positive;
- FN (False Negatives): The number of positive examples incorrectly classified as negative;
- TN (True Negatives): The number of negative examples correctly classified as negative.

The computation formulas for mAPval 0.5 and mAPval 0.5:0.95 are given below:

$$AP = \int_0^1 P(R)dR \tag{52}$$

$$mAP = \frac{\sum_{i=1}^{N} Pi}{N} \tag{53}$$

In the formulas, AP is derived by integrating the precision with respect to recall, whereas mAP is the mean of all individual AP values obtained for each object class. These metrics give a proper overall interpretation of the model performance regarding correct detection and classification of objects, knowing about the accuracy and stability attained across various IoUs. mAPval 0.5 stands for mean Average Precision evaluated based on detections with confidence scores greater than 0.5, computed using precision and recall at this threshold. The score thus demonstrates the model's acumen while operating at a fixed confidence threshold. Contrary to this, mAPval 0.5:0.95 determines average precision at a series of confidence thresholds generated between 0.5 and 0.95, at an increment of 0.05. Thus, with this quantity, one has a more standard sense of characterizing the model performance across varying confidence levels, particularly for assessing the detection confidence under certain test conditions.

The training and validation curves prototypes developed show the three distinct loss elements of interest, box loss, classification loss, and deformable loss. Box loss quantifies the accuracy at which the model localizes the center of each detected traffic sign so that the predicted bounding box advantages suitably cover it. The aim of classification loss is to quantify how accurately each object is classified within a given class. Deformable loss, introduced with the deformable convolution layer in YOLOv10, measures errors specific to these layers, which enhance detection performance for objects of various sizes and shapes. A lower dfl_loss indicates better handling of deformations and appearance variations, which is crucial for accurately detecting traffic signs from different viewing angles and under diverse conditions.

As shown in Fig. 9, precision, recall, and mAP values significantly improve after the initial 150 epochs, with stability reached around 220 epochs. This steady performance suggests that the YOLOv10-S model effectively learns the essential features for traffic sign detection, achieving an ideal balance between accuracy and efficiency for real-time applications.

6.3. Control Strategy Results

The PMSM parameters shown in Table 5 are adopted to demonstrate the effectiveness of the proposed control strategy. The developed controllers are compared with a PI controller [75], and an approach based on QLF [62]. Table 6 summarizes the PI controller gains obtained using different approaches. These gains were calculated by solving equations (19) and (42) in MATLAB, based on the LQR-based method outlined in Corollary 1 and the LILF-based method described in Corollary 2.

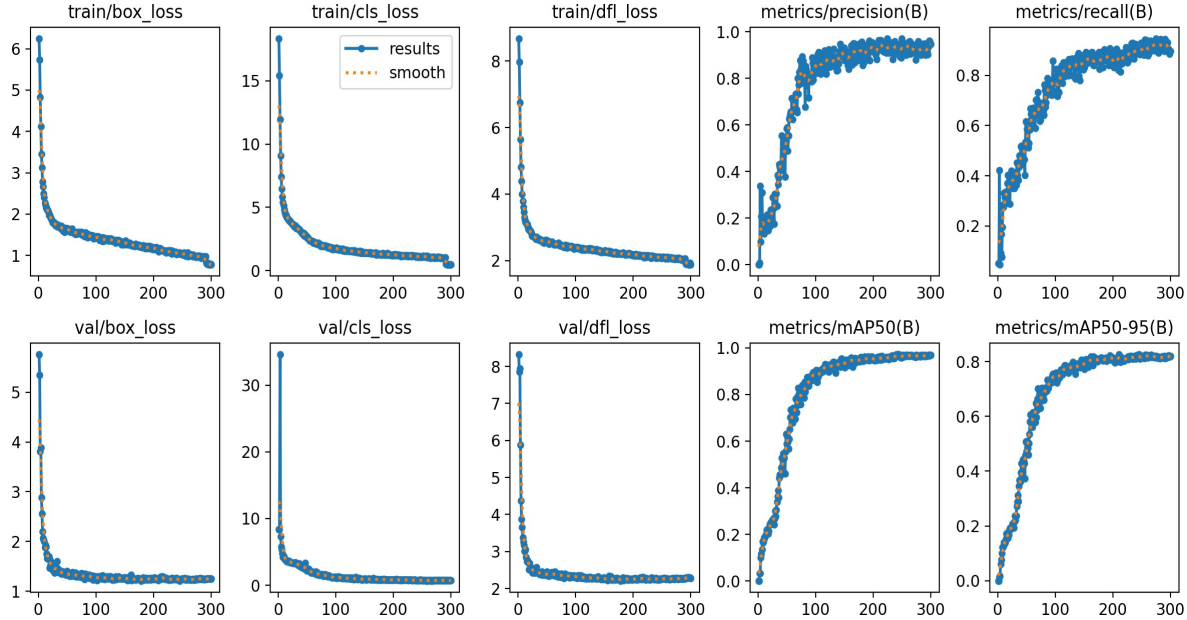

Fig. 9. Training and validation loss curves and performance metrics for YOLOv10-S model on traffic signs detection

Table 5. PMSM and vehicle parameters [62]

Parameters	Values
Stator resistance	$Rs = 2.875\ \Omega$
Direct axis inductance	$Ld = 7.5$ mH
Quadrature axis inductance	$Lq = 2.5$ mH
Moment of inertia	$J = 0.0008$ Kg
Coefficient of friction	$f = 10^{-4}$ N.m.s/rad
Flux linkage established by the PMSM	$\phi_m = 0.175$ Wb
Maximum PMSM rotor speed	$W_r^{max} = 1800$ rpm
Minimum PMSM rotor speed	$W_r^{min} = -1800$ rpm
Number of magnetic poles	$n_p = 8$

Table 6. Comparison of PID, LQR, QLF and LIFF controllers performs.

QLF	LILF	LQR	PID
$KP1^T = \begin{bmatrix} 5.778019200496586 & 1.374677294448111 \\ 11.758632188137721 & 2.433931532145648 \\ 6.427863135983328 & 14.384105977669797 \end{bmatrix}$	$KP1^T = \begin{bmatrix} 3.023868463991084 & 0.000000000000272 \\ 5.630585300187321 & 0.000000000000271 \\ -0.000000000000066 & 0.055762529323935 \end{bmatrix}$	$KP1^T = \begin{bmatrix} 3.023868463991084 & 0.000000000000272 \\ 5.630585300187321 & 0.000000000000271 \\ -0.000000000000066 & 0.055762529323935 \end{bmatrix}$	$KP = 38$
$KI1 = 1.0e+03 * \begin{bmatrix} 3.866412650413812 \\ 1.023900205415057 \end{bmatrix}$	$KI1 = 1.0e+03 * \begin{bmatrix} 1.645982546373085 \\ 0.000000000000292 \end{bmatrix}$	$KI1 = 1.0e+03 * \begin{bmatrix} 1.645982546373085 \\ 0.000000000000292 \end{bmatrix}$	$KI = 5.4$
$KP2^T = \begin{bmatrix} 5.778006348460579 & -1.374699072478540 \\ 11.758617083347531 & -2.433984098025249 \\ -6.427947045705971 & 14.384125144185177 \end{bmatrix}$	$KP2^T = \begin{bmatrix} 3.023868463983574 & 0.000000000000272 \\ 5.630585300179471 & 0.000000000000271 \\ -0.000000000000066 & 0.055762529323935 \end{bmatrix}$	$KP2^T = \begin{bmatrix} 3.023868463983574 & 0.000000000000272 \\ 5.630585300179471 & 0.000000000000271 \\ -0.000000000000066 & 0.055762529323935 \end{bmatrix}$	
$KI2 = 1.0e+03 * \begin{bmatrix} 3.866400683189616 \\ -1.023915547336438 \end{bmatrix}$	$KI2 = 1.0e+03 * \begin{bmatrix} 1.645982546365042 \\ 0.000000000000292 \end{bmatrix}$	$KI2 = 1.0e+03 * \begin{bmatrix} 1.645982546365042 \\ 0.000000000000292 \end{bmatrix}$	

To evaluate the effectiveness and performance of the proposed control strategies, Fig. 10 presents a comparative analysis of the vehicle's longitudinal speed tracking capability achieved with different controllers. More specifically, the figure illustrates the tracking performance of the reference speed

profile Vx using the proposed controllers, and compares the results with those obtained using a controller based on QLF and a conventional PI controller. The comparison highlights the ability of each control approach to track the desired velocity trajectory, with noticeable differences in responsiveness, accuracy, static error, and robustness to external disturbances. This evaluation provides valuable insights into the strengths and limitations of the proposed controllers relative to established control techniques in terms of precision, stability, and dynamic performance.

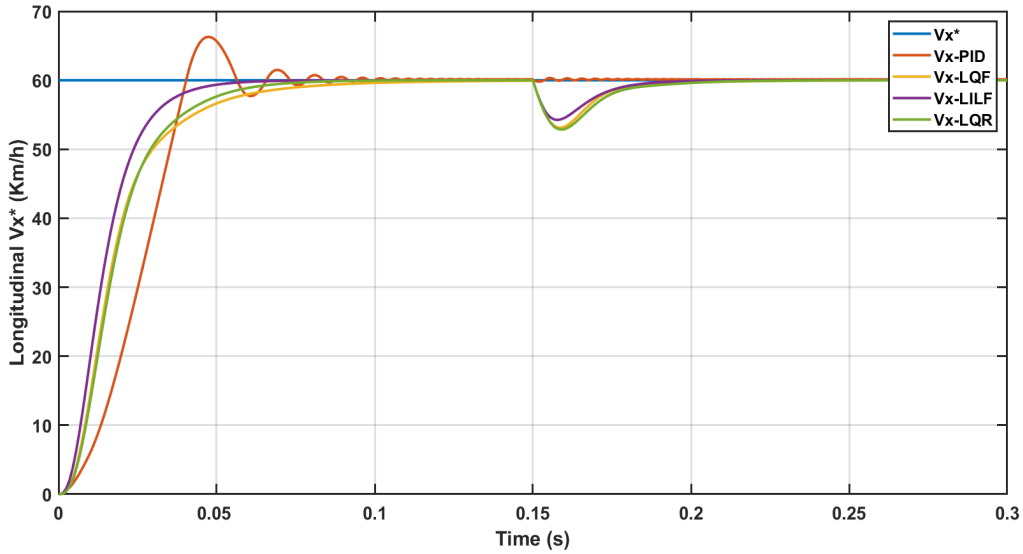

Fig. 10. Tracking longitudinal speed references $V_x{}^*(\mathrm{Km.\,h^{-1}})$

Moreover, it is well known that external disturbances can significantly degrade system performance and, in some cases, even lead to instability. To evaluate the robustness of the proposed control approaches, a step-form load torque disturbance of Cr=20 N. m, as shown in Fig. 11, is applied to the system at t=0.15s. For clarity, Table 7 compares the controllers' performance metrics.

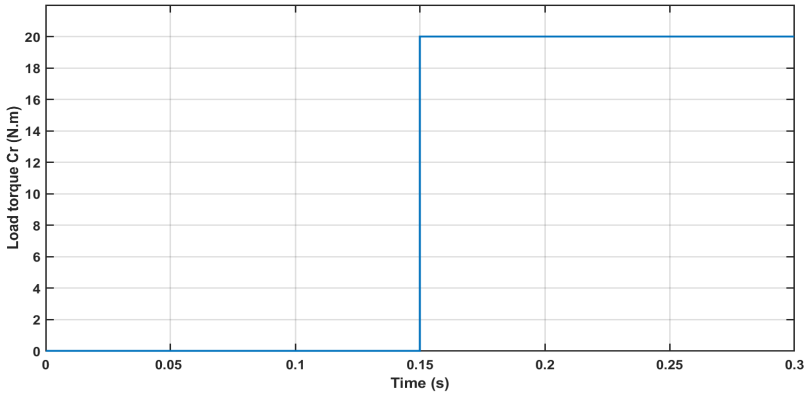

Fig. 11. Load torque profile (N.m)

Table 7. Comparison of PID, QLF and LIFF controllers performs

Performs type	LIFF	LQR	LQF	PID
Rise time (s) 10^{-3}	5	9	7	13
Overshoot %	0	0	0	24
Static error	0	0	0	0.25
Vibration	Absent	Absent	Absent	Exist
Response to disturbances	Very fast	Fast	Good	Good

Fig. 10 and the performance metrics in Table 7 clearly indicate that the LIFF controller delivers superior performance compared to all other methods. It demonstrates the fastest rise time (5 ms), zero overshoot, high tracking precision, and complete suppression of vibrations. While the QLF controller offers better rise time performance than the traditional LQR and PID controllers (7 ms for QLF, 9 ms for LQR, and 13 ms for PID), it proves less effective than the LQR controller in handling external disturbances.

It is important to note that the LQR controller is designed by considering an optimization trade-off between two objectives: accurate tracking of the speed $V_x{}^*$, associated with the state vector $x(t)$ and represented by the first term in equation (18), and minimizing energy consumption (current consumption), represented by the second term involving the control input $u(t)$. This balance is particularly critical in the transient regime, and where the system's response to disturbances is most significant. The PID controller shows the weakest performance overall, with the slowest rise time, the highest static error (0.25), a 24% overshoot, and noticeable oscillations. Additionally, Its poor disturbance rejection results in greater system vibrations under load changes.

According to the context of this work, which involves adopting small values of slip angle, the engine must rotate at a specific angular speed, denoted as $W_r{}^*$, which corresponds to the reference longitudinal speed of the vehicle, denoted as $V_x{}^*$. Consequently, Fig. 12 shows that the angular speed W_r follows the same dynamics as the longitudinal speed V_x, but with a proportionality coefficient that precedes it.

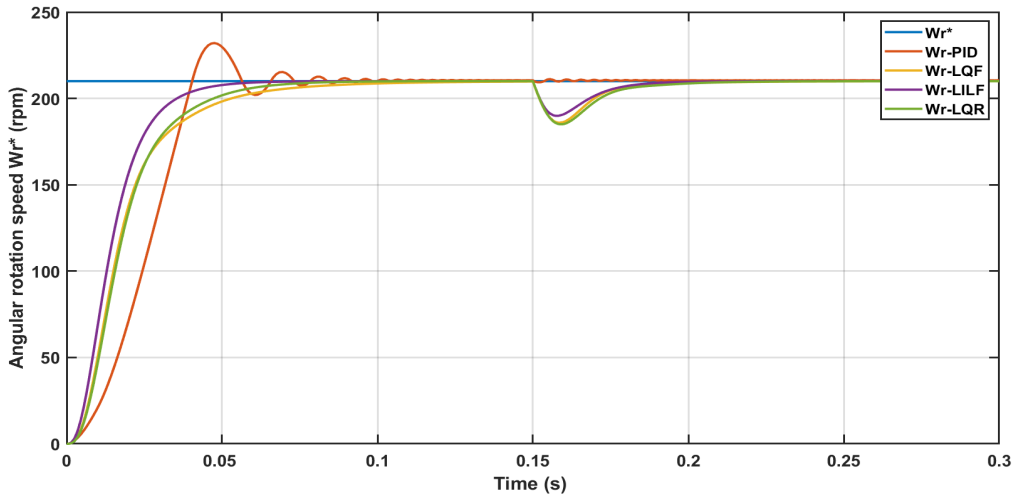

Fig. 12. Tracking angular rotation speed references $W^*(\mathrm{Km.\,h^{-1}})$

Fig. 13 and Fig. 14 show that the LQR-based controller achieves the lowest current consumption among all the control methods, in both the Iq and Id components. This result aligns with the objective function defined in (18), which prioritizes a balance between accurate reference tracking and minimal power consumption, as previously discussed. The LIFF controller ranks second in terms of steady-state current consumption, as clearly illustrated in Fig. 14. However, during the transient phase, its faster response to the reference signal leads to higher current consumption compared to the other controllers. Additionally, the LQR, LIFF, and QLF controllers generate smoother current profiles than the traditional PI controller.

Fig. 15 shows the variation of the electromagnetic torque generated by the motor. According to (7), these results are specifically related to the Iq component of the current, which has a direct impact on torque production. Moreover, the presence of non-smooth current, containing high-frequency harmonics, leads to abrupt fluctuations in the generated torque. These variations induce vibrations in the motor, which are then transmitted to the vehicle, thereby increasing the overall vibration levels.

Additionally, the application of this perturbation will force the motor to develop a more powerful electromagnetic torque to compensate for the effect of this perturbation, and consequently to absorb more current, which justifies the variation in the current components (Fig. 13 and Fig. 14) and torque Fig. 15, at the moment of application of this perturbation.

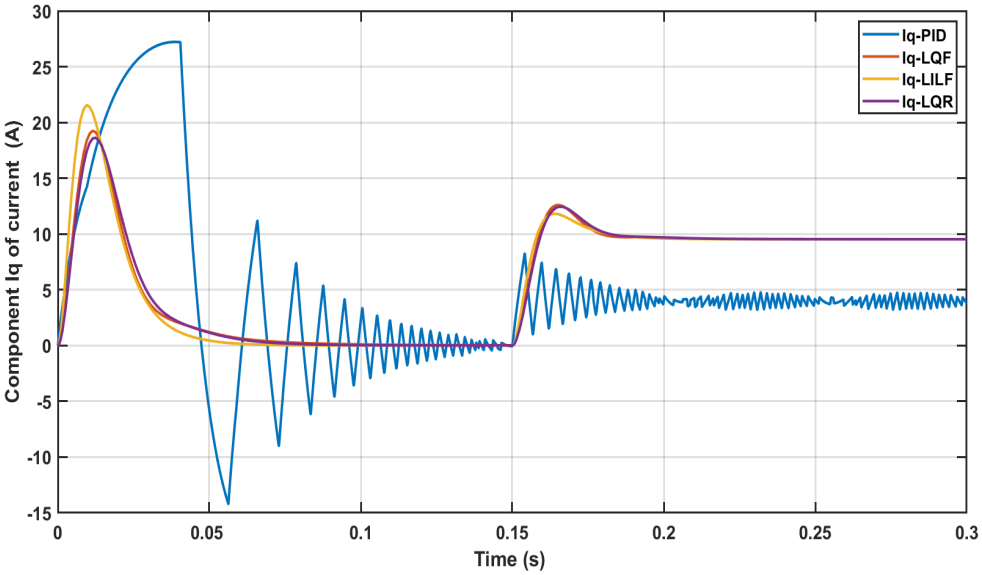

Fig. 13. Variation of I_q (A) current components

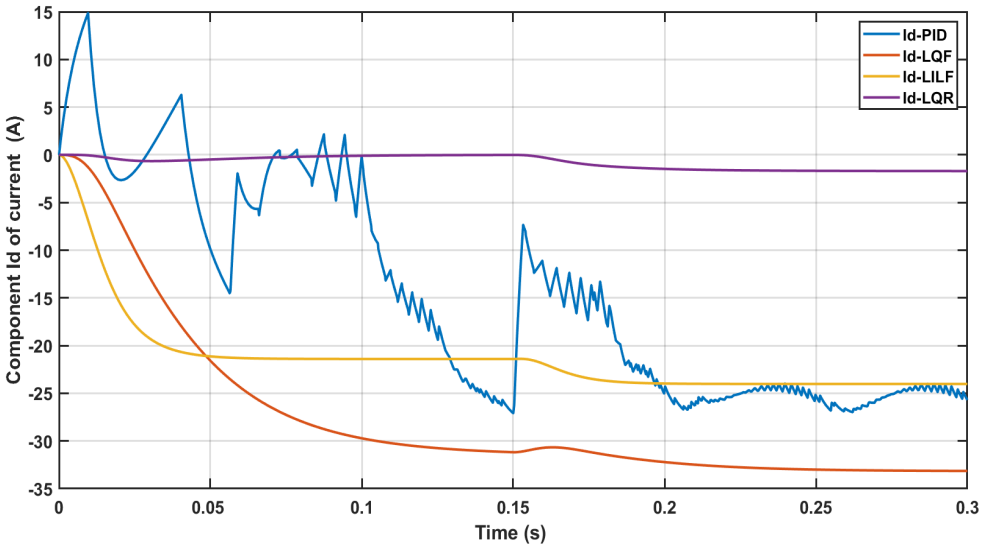

Fig. 14. Variation of I_d (A) current components

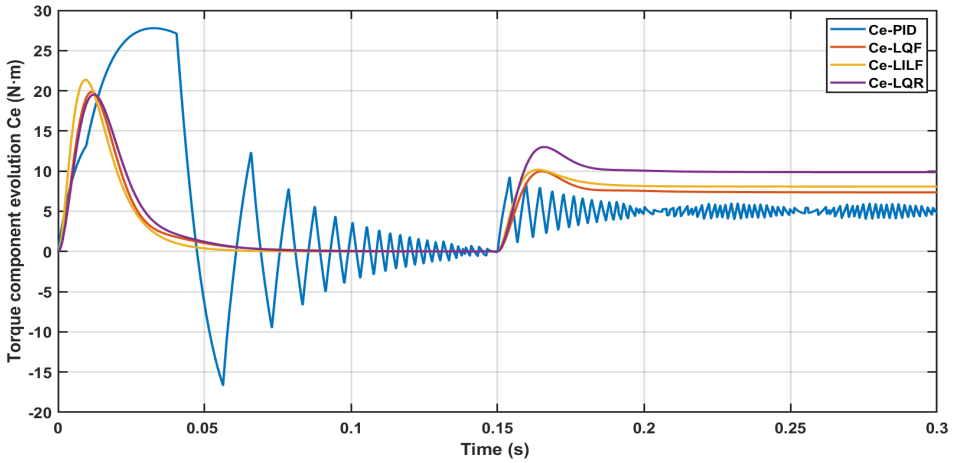

Fig. 15. Torque variation C_e (N.m)

During autonomous vehicle (AV) operation in real-world conditions, an onboard camera continuously captures images of the road. These images are processed in real time by a YOLOv10-based algorithm, which detects and recognizes speed limit signs. The identified speed limit is then compared with the vehicle's current speed. If a mismatch is detected, a control system intervenes to adjust the engine inputs, ensuring that the vehicle's speed complies with the detected speed limit. To perform this function effectively, the controller must dynamically respond to changes in the target speed $V_x{}^*$, adapting to varying speed commands. As a result, the engine must produce a torque suited to each new driving condition. Fig. 16 illustrates a desired speed profile. The comparison shows that all controllers are capable of accurately tracking the reference speed $V_x{}^*$. However, the traditional PI controller displays noticeable oscillations, as previously noted.

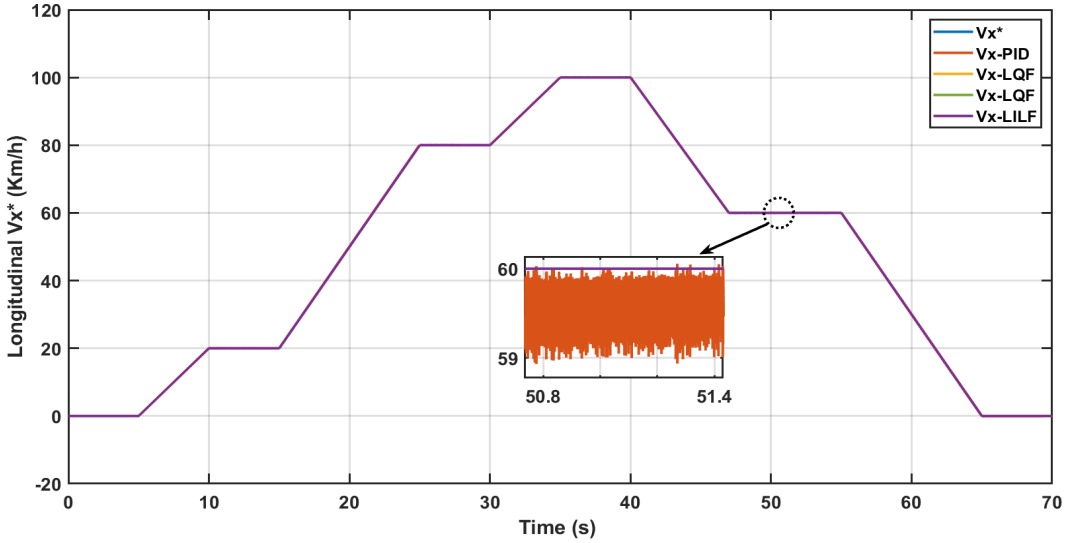

Fig. 16. Tracking longitudinal speed references V_x*(Km. h^{-1})

7. Conclusion

This research proposes a control strategy for autonomous vehicles, integrating advanced methodologies in computer vision and control to enhance safety and operational performance. Based on the YOLOv10 algorithm, the system enables accurate and real-time detection of speed limit signs, thereby allowing for the effective definition of dynamic target speeds under realistic traffic conditions. The integration of this perception layer with a fuzzy PI controller enables robust and smooth regulation of the vehicle's motor, modeled as a PMSM, without the need for local linearization or precise

parameter estimation. To compute the fuzzy PI controller parameters, two approaches were employed. In the first approach, the problem was formulated as an LQR problem, where the goal is to optimize a cost function that ensures speed tracking while minimizing energy consumption. In the second approach, an H∞ method combined with an LILF was used to formulate LMI constraints to be solved.

Simulation results validate the proposed approach, demonstrating its superiority over conventional control methods in minimizing speed and torque ripples, while ensuring strong disturbance rejection and high adaptability. This study provides a promising foundation for the development of intelligent and efficient speed regulation systems for autonomous vehicles. Future work will focus on investigating the impact of a leading vehicle's presence, as in such scenarios the velocity detected by YOLOv10 may not always meet safety requirements, requiring enhanced perception and control strategies.

Author Contribution: All authors contributed equally to the main contributor to this paper. All authors read and approved the final paper.

Funding: This research received no external funding.

Conflicts of Interest: The authors declare no conflict of interest.

References

[1] M. Shamsuddoha, M. A. Kashem, and T. Nasir, "A review of transportation 5.0: Advancing sustainable mobility through intelligent technology and renewable energy," *Future Transportation*, vol. 5, no. 1, p. 8, 2025, https://doi.org/10.3390/futuretransp5010008.

[2] World Health Organization, *Global status report on road safety 2023: summary*, Geneva: World Health Organization, 2023, https://www.who.int/publications/i/item/9789240086456.

[3] E. Elouardi, L. Sellak, C. El Mokhi, Y. Adnani, L. Idkhajine, B. El Ouardi, and O. Mouhib, "Lateral control for autonomous vehicles utilizing an ANN-based controller," in *2024 10th International Conference on Optimization and Applications (ICOA)*, 2024, pp. 1–5, https://doi.org/10.1109/ICOA62581.2024.10754161.

[4] M. Zarboubi, S. Chabaa, and A. Dliou, "Advancing precision agriculture with deep learning and IoT integration for effective tomato pest management," in *2023 IEEE International Conference on Advances in Data-Driven Analytics and Intelligent Systems (ADACIS)*, 2023, pp. 1–6, https://doi.org/10.1109/ADACIS59737.2023.10424149.

[5] M. Zarboubi, S. Chabaa, A. Dliou, and A. Zeroual, "Smart pest control in grain warehouses: YOLOv8-powered IoT robot car for precision agriculture," in *2024 International Conference on Global Aeronautical Engineering and Satellite Technology (GAST)*, 2024, pp. 1–6, https://doi.org/10.1109/GAST60528.2024.10520743.

[6] A. Raj, C. Mishra, S. Joga, I. M. Elzein, A. Mohanty, S. Ika, M. Mahmoud, and A. Ewais, "Wavelet analysis–singular value decomposition based method for precise fault localization in power distribution networks using k-NN classifier," *International Journal of Robotics and Control Systems*, vol. 5, no. 1, pp. 530–554, 2025, https://doi.org/10.31763/ijrcs.v5i1.1543.

[7] J. Redmon and A. Farhadi, "YOLOv3: An incremental improvement," *arXiv preprint,* arXiv:1804.02767, 2018, https://arxiv.org/abs/1804.02767.

[8] W. Liu, D. Anguelov, D. Erhan, C. Szegedy, S. Reed, C.-Y. Fu, and A. C. Berg, "SSD: Single shot multibox detector," in *Computer Vision – ECCV 2016*, B. Leibe, J. Matas, N. Sebe, and M. Welling, Eds. Cham: Springer International Publishing, 2016, pp. 21–37, https://doi.org/10.1007/978-3-319-46448-0_2.

[9] Z. Cai and N. Vasconcelos, "Cascade R-CNN: Delving into high quality object detection," in *2018 IEEE/CVF Conference on Computer Vision and Pattern Recognition*, 2018, pp. 6154–6162, https://doi.org/10.1109/CVPR.2018.00644.

[10] S. Ren, K. He, R. Girshick, and J. Sun, "Faster R-CNN: Towards real-time object detection with region proposal networks," *IEEE Transactions on Pattern Analysis and Machine Intelligence*, vol. 39, no. 6, pp. 1137–1149, 2017, https://doi.org/10.1109/TPAMI.2016.2577031.

[11] R. Girshick, "Fast R-CNN," in *2015 IEEE International Conference on Computer Vision (ICCV)*, 2015, pp. 1440–1448, https://doi.org/10.1109/ICCV.2015.169.

[12] Z. Liu, M. Qi, C. Shen, Y. Fang, and X. Zhao, "Cascade saccade machine learning network with hierarchical classes for traffic sign detection," *Sustainable Cities and Society*, vol. 67, p. 102700, 2021, https://doi.org/10.1016/j.scs.2020.102700 .

[13] W. Huang, L. Zhang, W. Gao, F. Min, and J. He, "Shallow convolutional neural networks for human activity recognition using wearable sensors," *IEEE Transactions on Instrumentation and Measurement*, vol. 70, pp. 1–11, 2021, https://doi.org/10.1109/TIM.2021.3091990.

[14] M. Flores-Calero, C. A. Astudillo, D. Guevara, J. Maza, B. S. Lita, B. Defaz, J. S. Ante, D. Zabala-Blanco, and J. M. Armingol Moreno, "Traffic sign detection and recognition using YOLO object detection algorithm: A systematic review," *Mathematics*, vol. 12, no. 2, p. 297, 2024, https://doi.org/10.3390/math12020297.

[15] J. Redmon, S. Divvala, R. Girshick, and A. Farhadi, "You only look once: Unified, real-time object detection," in *2016 IEEE Conference on Computer Vision and Pattern Recognition (CVPR)*, 2016, pp. 779–788, https://doi.org/10.1109/CVPR.2016.91.

[16] J. Redmon and A. Farhadi, "YOLO9000: Better, faster, stronger," in *2017 IEEE Conference on Computer Vision and Pattern Recognition (CVPR)*, 2017, pp. 6517–6525, https://doi.org/10.1109/CVPR.2017.690.

[17] A. Bochkovskiy, C.-Y. Wang, and H.-Y. M. Liao, "YOLOv4: Optimal speed and accuracy of object detection," *arXiv preprint,* arXiv:2004.10934, 2020, https://arxiv.org/abs/2004.10934.

[18] G. Jocher, A. Stoken, J. Borovec, NanoCode012, ChristopherSTAN, C. Liu, Laughing, A. Hogan, lorenzomammana, tkianai, yxNONG, AlexWang1900, L. Diaconu, Marc, wanghaoyang0106, ml5ah, Doug, Hatovix, J. Poznanski, L. Yu, changyu98, P. Rai, R. Ferriday, T. Sullivan, X. Wang, YuriRibeiro, E. R. Claramunt, hopesala, pritul dave, and yzchen, "ultralytics/yolov5: v3.0," *Zenodo*, Aug. 2020, https://doi.org/10.5281/zenodo.3983579.

[19] C. Li, L. Li, H. Jiang, K. Weng, Y. Geng, L. Li, Z. Ke, Q. Li, M. Cheng, W. Nie, Y. Li, B. Zhang, Y. Liang, L. Zhou, X. Xu, X. Chu, X. Wei, and X. Wei, "YOLOv6: A single-stage object detection framework for industrial applications," *arXiv preprint,* arXiv:2209.02976, 2022, https://arxiv.org/abs/2209.02976.

[20] C.-Y. Wang, A. Bochkovskiy, and H.-Y. M. Liao, "YOLOv7: Trainable bag-of-freebies sets new state-of-the-art for real-time object detectors," in *Proceedings of the IEEE/CVF Conference on Computer Vision and Pattern Recognition (CVPR)*, 2023, pp. 7464–7475, https://doi.org/10.1109/CVPR52729.2023.00721.

[21] Z. Huang, L. Li, G. Krizek, and L. Sun, "Research on traffic sign detection based on improved YOLOv8," *Journal of Computer and Communications*, vol. 11, pp. 226–232, 2023, https://doi.org/10.4236/jcc.2023.117014.

[22] C.-Y. Wang, I.-H. Yeh, and H.-Y. M. Liao, "YOLOv9: Learning what you want to learn using programmable gradient information," in *Computer Vision – ECCV 2024*, A. Leonardis, E. Ricci, S. Roth, O. Russakovsky, T. Sattler, and G. Varol, Eds. Cham: Springer Nature Switzerland, 2025, pp. 1–21. https://doi.org/10.1007/978-3-031-72751-1_1.

[23] A. Wang, H. Chen, L. Liu, K. Chen, Z. Lin, J. Han, and G. Ding, "YOLOv10: Real-Time End-to-End Object Detection," *arXiv preprint*, arXiv.2405.14458, 2024, https://doi.org/10.48550/arXiv.2405.14458.

[24] F. Filippi, "A paradigm shift for a transition to sustainable urban transport," *Sustainability*, vol. 14, no. 5, p. 2853, 2022. https://doi.org/10.3390/su14052853.

[25] B. Benbouya, H. Cheghib, M. Behim, M. Mahmoud, M. F. Elnaggar, N. Ibrahim, and N. Anwer, "Dynamic assessment and control of a dual star induction machine state dedicated to an electric vehicle under short-circuit defect," *International Journal of Robotics and Control Systems*, vol. 4, no. 4, pp. 1731–1745, 2024, https://doi.org/10.31763/ijrcs.v4i4.1557.

[26] Y. Maamar, I. Elzein, H. Alnami, B. Brahim, A. Benameur, H. Mohamed, and M. Mahmoud, "Design, modeling, and simulation of a new adaptive backstepping controller for permanent magnet linear synchronous motor: A comparative analysis," *International Journal of Robotics and Control Systems*, vol. 5, no. 1, pp. 296–310, 2024, https://doi.org/10.31763/ijrcs.v5i1.1425.

[27] I. M. Elzein, Y. Maamar, M. M. Mahmoud, M. I. Mosaad, and S. A. Shaaban, "The utilization of a TSR-MPPT-based backstepping controller and speed estimator across varying intensities of wind speed turbulence," *International Journal of Robotics and Control Systems*, vol. 5, no. 2, pp. 1315–1330, May 2025, https://doi.org/10.31763/ijrcs.v5i2.1793.

[28] T. Boutabba, I. Benlaloui, F. Mechnane, I. M. Elzein, A. Ma'arif, A. M. Hassan, and M. Mahmoud, "Design of a small wind turbine emulator for testing power converters using dSPACE 1104," *International Journal of Robotics and Control Systems*, vol. 5, no. 2, pp. 698–712, 2025, https://doi.org/10.31763/ijrcs.v5i2.1685.

[29] X. Wu, W. Song, and C. Xue, "Low-complexity model predictive torque control method without weighting factor for five-phase PMSM based on hysteresis comparators," *IEEE Journal of Emerging and Selected Topics in Power Electronics*, vol. 6, no. 4, pp. 1650–1661, Dec. 2018, https://doi.org/10.1109/JESTPE.2018.2849320.

[30] M. Bermudez, I. Gonzalez-Prieto, F. Barrero, H. Guzman, M. J. Duran, and X. Kestelyn, "Open-phase fault-tolerant direct torque control technique for five-phase induction motor drives," *IEEE Transactions on Industrial Electronics*, vol. 64, no. 2, pp. 902–911, Feb. 2017, https://doi.org/10.1109/TIE.2016.2610941.

[31] R. Bousseksou, N. Bessous, I. M. Elzein, M. Mahmoud, A. Ma'arif, E. Touti, A. Al-Quraan, and N. Anwer, "Utilizing short-time Fourier transform for the diagnosis of rotor bar faults in induction motors under direct torque control," *International Journal of Robotics and Control Systems*, vol. 5, no. 2, pp. 1441–1457, 2025, https://doi.org/10.31763/ijrcs.v5i2.1886.

[32] H. Xu, H. A. Toliyat, and L. J. Petersen, "Resilient current control of five-phase induction motor under asymmetrical fault conditions," in *APEC. Seventeenth Annual IEEE Applied Power Electronics Conference and Exposition*, Dallas, USA, 2002, pp. 64–71, https://doi.org/10.1109/APEC.2002.989228.

[33] K. Iffouzar, M. F. F. Benkhoris, H. Aouzellag, K. Ghedamsi, and D. Aouzellag, "Direct rotor field oriented control of polyphase induction machine based on fuzzy logic controller," *Revue Roumaine des Sciences Techniques, Série Électrotechnique et Énergétique*, vol. 62, no. 1, pp. 42–47, Apr. 2017, https://www.researchgate.net/publication/315740220_Direct_rotor_field_oriented_control_of_polyphase_induction_machine_based_on_fuzzy_logic_controller.

[34] O. Lamine, N. Bessous, B. Abdelhalim, F. A. Banakhr, M. I. Mosaad, M. Oussama, and M. Mahmoud, "A combination of INC and fuzzy logic-based variable step size for enhancing MPPT of PV systems," *International Journal of Robotics and Control Systems*, vol. 4, no. 2, pp. 877–892, 2024. https://doi.org/10.31763/ijrcs.v4i2.1428.

[35] H. Guzman, M. J. Duran, F. Barrero, L. Zarri, B. Bogado, I. Gonzalez Prieto, and M. R. Arahal, "Comparative study of predictive and resonant controllers in fault-tolerant five-phase induction motor drives," *IEEE Transactions on Industrial Electronics*, vol. 63, no. 1, pp. 606–617, 2016, https://doi.org/10.1109/TIE.2015.2418732.

[36] S. Lee, T. Lemley, and G. Keohane, "A comparison study of the commutation methods for the three-phase permanent magnet brushless DC motor," in *Electrical Manufacturing Technical Conference 2009: Electrical Manufacturing and Coil Winding Expo*, 2009, pp. 49–55,

https://pure.psu.edu/en/publications/a-comparison-study-of-the-commutation-methods-for-the-three-phase/.

[37] P. S. Chaudhari, S. L. Patil, S. K. Pandey, and S. Sinha, "Performance analysis of BLDC motor on sinusoidal and square wave supply," in *2016 IEEE International Conference on Power Electronics, Drives and Energy Systems (PEDES)*, Trivandrum, India, 2016, pp. 1–6, https://doi.org/10.1109/PEDES.2016.7914354.

[38] V. Trifa, G. Brezeanu, and E. Ceuca, "Block commutation vs sinusoidal commutation for BLDC motors," in *2020 International Semiconductor Conference (CAS)*, Sinaia, Romania, 2020, pp. 89–92, https://doi.org/10.1109/CAS50358.2020.9268018.

[39] C.-L. Huang, G.-R. Chen, S.-C. Yang, and Y.-L. Hsu, "Comparison of high speed permanent magnet machine sensorless drive using trapezoidal BLDC and sinusoidal FOC under insufficient PWM frequency," in *2019 IEEE Energy Conversion Congress and Exposition (ECCE)*, 2019, pp. 321–325, https://doi.org/10.1109/ECCE.2019.8912495.

[40] K. Kolano, "New method of vector control in PMSM motors," *IEEE Access*, vol. 11, pp. 43882–43890, 2023, https://doi.org/10.1109/ACCESS.2023.3272273.

[41] M.-F. Hsieh, N.-C. Chen, and T.-D. Ton, "System response of permanent magnet synchronous motor drive based on SiC power transistor," in *2019 IEEE 4th International Future Energy Electronics Conference (IFEEC)*, Singapore, 2019, pp. 1–6, https://doi.org/10.1109/IFEEC47410.2019.9015197.

[42] G. Zhang, G. Wang, D. Xu, and Y. Yu, "Discrete-time low-frequency-ratio synchronous-frame full-order observer for position sensorless IPMSM drives," *IEEE Journal of Emerging and Selected Topics in Power Electronics*, vol. 5, no. 2, pp. 870–879, Jun. 2017, https://doi.org/10.1109/JESTPE.2017.2659719.

[43] S. N. Vukosavic, L. S. Peric, and E. Levi, "Digital current controller with error-free feedback acquisition and active resistance," *IEEE Transactions on Industrial Electronics*, vol. 65, no. 3, pp. 1980–1990, Mar. 2018, https://doi.org/10.1109/TIE.2017.2745476.

[44] X. Sun, T. Li, Z. Zhu, G. Lei, Y. Guo, and J. Zhu, "Speed sensorless model predictive current control based on finite position set for PMSHM drives," *IEEE Transactions on Transportation Electrification*, vol. 7, no. 4, pp. 2743–2752, Dec. 2021, https://doi.org/10.1109/TTE.2021.3081436.

[45] X. Sun, T. Li, M. Yao, G. Lei, Y. Guo, and J. Zhu, "Improved finite-control-set model predictive control with virtual vectors for PMSHM drives," *IEEE Transactions on Energy Conversion*, pp. 1–1, 2021, https://doi.org/10.1109/TEC.2021.3138905.

[46] M. Fodil, A. Djerioui, M. Ladjal, A. Saim, F. Berrabah, H. Mekki, S. Zeghlache, A. Houari, and M. F. Benkhoris, "Optimization of PI controller parameters by GWO algorithm for five-phase asynchronous motor," *Energies*, vol. 16, no. 10, p. 4251, 2023, https://doi.org/10.3390/en16104251.

[47] E. Elouardi, I. Lagrat, O. Mouhib, A. Bentaleb, and E. Brahim, "Fuzzy-PI controller using line integral Lyapunov fuzzy function: Application to electric vehicle powered by PMSM motor," in *Intelligent Systems and Advanced Computing Sciences*, H. Hagras, Y. Bennani, and M. Nemiche, Eds. Cham, Switzerland: Springer Nature, 2025, pp. 265–277, https://doi.org/10.1007/978-3-031-93448-3_22.

[48] Y. Bekakra and D. B. Attous, "Optimizing of IP speed controller using particle swarm optimization for FOC of an induction motor," *International Journal of System Assurance Engineering and Management*, vol. 8, no. S1, pp. 361–369, Jan. 2017, https://doi.org/10.1007/s13198-015-0391-1.

[49] O. P. Bharti, R. K. Saket, and S. K. Nagar, "Controller design for doubly fed induction generator using particle swarm optimization technique," *Renewable Energy*, vol. 114, pp. 1394–1406, Dec. 2017, https://doi.org/10.1016/j.renene.2017.06.061.

[50] W. Zhihong, L. Gensheng, Z. Yuan, T. Guangyu, and L. Ke, "A new nonlinear PI controller of permanent magnet synchronous motor," in *2010 Second International Conference on Intelligent Human-Machine Systems and Cybernetics*, Nanjing, China, Aug. 2010, pp. 99–102, https://doi.org/10.1109/IHMSC.2010.32.

[51] U. Thakar, V. Joshi, and V. Vyawahare, "Design of fractional-order PI controllers and comparative analysis of these controllers with linearized, nonlinear integer-order and nonlinear fractional-order representations of PMSM," *International Journal of Dynamics and Control*, vol. 5, no. 1, pp. 187–197, Mar. 2017, https://doi.org/10.1007/s40435-016-0243-0.

[52] P. Q. Khanh and H. P. H. Anh, "Improved PMSM speed control using fuzzy PI method for hybrid active and reactive power control approach," in *Computational Intelligence Methods for Green Technology and Sustainable Development*, Y.-P. Huang, W.-J. Wang, H. A. Quoc, H.-G. Le, and H.-N. Quach, Eds., *Lecture Notes in Networks and Systems*, vol. 567. Cham: Springer International Publishing, 2023, pp. 345–356, https://doi.org/10.1007/978-3-031-19694-2_31.

[53] Señales de Tráfico y Su Significado — Experto en Siniestros, https://senalesdetraficoinfo.es/.

[54] P. Jiang, D. Ergu, F. Liu, Y. Cai, and B. Ma, "A review of YOLO algorithm developments," *Procedia Computer Science*, vol. 199, pp. 1066–1073, 2022, https://doi.org/10.1016/j.procs.2022.01.135.

[55] A. Gupta, A. Anpalagan, L. Guan, and A. S. Khwaja, "Deep learning for object detection and scene perception in self-driving cars: Survey, challenges, and open issues," *Array*, vol. 10, p. 100057, Jul. 2021, https://doi.org/10.1016/j.array.2021.100057.

[56] T. Diwan, G. Anirudh, and J. V. Tembhurne, "Object detection using YOLO: challenges, architectural successors, datasets and applications," *Multimedia Tools and Applications*, vol. 82, no. 6, pp. 9243–9275, Mar. 2023, https://doi.org/10.1007/s11042-022-13644-y.

[57] A. Boukerche and Z. Hou, "Object detection using deep learning methods in traffic scenarios," *ACM Computing Surveys*, vol. 54, no. 2, pp. 1–35, Mar. 2022, https://doi.org/10.1145/3434398.

[58] M. Yılmaz and S. Ozdemir, "Review of motors used in commercial electric vehicles," in *5th International Mediterranean Science and Engineering Congress (IMSEC 2020)*, Antalya, Turkey, Oct. 2020, https://www.researchgate.net/publication/348153072_Review_of_Motors_used_in_Commercial_Electric_Vehicles.

[59] S. J. Rind, Y. Ren, Y. Hu, J. Wang, and L. Jiang, "Configurations and control of traction motors for electric vehicles: A review," *Chinese Journal of Electrical Engineering*, vol. 3, no. 3, pp. 1–17, Dec. 2017, https://doi.org/10.23919/CJEE.2017.8250419.

[60] D. Rimpas, S. D. Kaminaris, D. D. Piromalis, G. Vokas, K. G. Arvanitis, and C.-S. Karavas, "Comparative review of motor technologies for electric vehicles powered by a hybrid energy storage system based on multi-criteria analysis," *Energies*, vol. 16, no. 6, p. 2555, Jan. 2023, https://doi.org/10.3390/en16062555.

[61] B. Sarlioglu, C. T. Morris, D. Han, and S. Li, "Driving toward accessibility: A review of technological improvements for electric machines, power electronics, and batteries for electric and hybrid vehicles," *IEEE Industrial Applications Magazine*, vol. 23, no. 1, pp. 14–25, Jan. 2017, https://doi.org/10.1109/MIAS.2016.2600739.

[62] E. Elouardi, O. Mouhib, A. Bentaleb, B. E. Ouardi, A. Lassioui, and H. E. Fadil, "Cruise control system of electric vehicle powered by PMSM motor using T-S fuzzy approach," in *Automatic Control and Emerging Technologies*, H. El Fadil and W. Zhang, Eds., Singapore: Springer Nature, 2024, pp. 726–735, https://doi.org/10.1007/978-981-97-0126-1_64.

[63] M. Megrini, A. Gaga, and Y. Mehdaoui, "Review of electric vehicle traction motors, control systems, and various implementation cards," *Journal of Operation and Automation in Power Engineering*, vol. 13, no. 3, pp. 238–247, Aug. 2025, http://joape.uma.ac.ir/article_2942_3d1130a05b2ba124185177270fc0bc39.pdf.

[64] S. Madichetty, S. Mishra, and M. Basu, "New trends in electric motors and selection for electric vehicle propulsion systems," *IET Electrical Systems in Transportation*, vol. 11, no. 3, pp. 186–199, 2021, https://doi.org/10.1049/els2.12018.

[65] E. Agamloh, A. von Jouanne, and A. Yokochi, "An overview of electric machine trends in modern electric vehicles," *Machines*, vol. 8, no. 2, p. 20, Jun. 2020, https://doi.org/10.3390/machines8020020.

[66] Z. Wang, T. W. Ching, S. Huang, H. Wang, and T. Xu, "Challenges faced by electric vehicle motors and their solutions," *IEEE Access*, vol. 9, pp. 5228–5249, 2021, https://doi.org/10.1109/ACCESS.2020.3045716.

[67] T. Takagi and M. Sugeno, "Fuzzy identification of systems and its applications to modeling and control," *IEEE Transactions on Systems, Man, and Cybernetics*, vol. SMC-15, no. 1, pp. 116–132, Jan. 1985, https://doi.org/10.1109/TSMC.1985.6313399.

[68] D. Ounnas, S. Chenikher, and T. Bouktir, "Tracking control for permanent magnet synchronous machine based on Takagi-Sugeno fuzzy models," in *2013 Eighth International Conference and Exhibition on Ecological Vehicles and Renewable Energies (EVER)*, Mar. 2013, pp. 1–5, https://doi.org/10.1109/EVER.2013.6521548.

[69] H. Kheloufi, A. Zemouche, F. Bedouhene, and M. Boutayeb, "On LMI conditions to design observer-based controllers for linear systems with parameter uncertainties," *Automatica*, vol. 49, no. 12, pp. 3700–3704, Dec. 2013, https://doi.org/10.1016/j.automatica.2013.09.046.

[70] H. Dahmani, O. Pagès, A. El Hajjaji, and N. Daraoui, "Observer-based tracking control of the vehicle lateral dynamics using four-wheel active steering," in *16th International IEEE Conference on Intelligent Transportation Systems (ITSC 2013)*, Oct. 2013, pp. 360–365, https://doi.org/10.1109/ITSC.2013.6728258..

[71] J. M. Saenz, M. Tanaka, and K. Tanaka, "Relaxed stabilization and disturbance attenuation control synthesis conditions for polynomial fuzzy systems," *IEEE Transactions on Cybernetics*, vol. 51, no. 4, pp. 2093–2106, 2021, https://doi.org/10.1109/TCYB.2019.2957154.

[72] R. Houili, M. Y. Hammoudi, M. Benbouzid, and A. Titaouine, "Observer-based controller using line integral Lyapunov fuzzy function for TS fuzzy systems: Application to induction motors," *Machines*, vol. 11, no. 3, p. 374, Mar. 2023, https://doi.org/10.3390/machines11030374.

[73] B.-J. Rhee and S. Won, "A new fuzzy Lyapunov function approach for a Takagi-Sugeno fuzzy control system design," *Fuzzy Sets and Systems*, vol. 157, no. 9, pp. 1211–1228, May 2006, https://doi.org/10.1016/j.fss.2005.12.020.

[74] N. Vafamand, "Global non-quadratic Lyapunov-based stabilization of T-S fuzzy systems: A descriptor approach," *Journal of Vibration and Control*, vol. 26, no. 19–20, pp. 1765–1778, Oct. 2020, https://doi.org/10.1177/1077546320904817.

[75] K. Cherif, A. Sahbani, and K. B. Saad, "Performance evaluation of PI and sliding mode control for PMSM in applications for electric vehicles," *Engineering, Technology & Applied Science Research*, vol. 14, no. 4, pp. 15464–15470, Aug. 2024, https://doi.org/10.48084/etasr.7172.